Spring 2019

Atomistic simulations of deformation in Metallic Nanolayered Composites

Sixie Huang

Department: Materials Science and Engineering

ATOMISTIC SIMULATIONS OF DEFORMATION IN METALLIC NANOLAYERED COMPOSITES

by

SIXIE HUANG

A DISSERTATION

Presented to the Faculty of the Graduate School of the

MISSOURI UNIVERSITY OF SCIENCE AND TECHNOLOGY

In Partial Fulfillment of the Requirements for the Degree

DOCTOR OF PHILOSOPHY

in

MATERIALS SCIENCES AND ENGINEERING

2019

Approved by

Dr. Caizhi Zhou, Advisor
Dr. Matthew O'Keefe
Dr. David Van Aken
Dr. Mohsen Asle Zaeem
Dr. Xiaoping Du

PUBLICATION DISSERTATION OPTION

This dissertation consists of the following three articles that have been published or submitted for publication as follows:

Paper I, pages 25-48 have been published in Scientific Reports, Volume 7: 11251, 2017.

Paper II, pages 49-68 have been submitted in Journal of Materials Research.

Paper III, pages 69-83 have been published in Materials Science & Engineering: A, 636: 430-433, 2015

An introduction, a literature review, molecular dynamics fundamentals and dislocation dynamics fundamentals have been added to provide supplemental information.

ABSTRACT

The mechanical behavior of Metallic Nanolayered Composites (MNCs) is governed by their underlying microstructure. In this dissertation, the roles of the interlayer spacing (grain size, *d*) and the intralayer biphase spacing (layer thickness, *h*) on mechanical response of Cu/Nb MNCs are examined by Molecular Dynamics (MD) simulations.

The study of the strength of MNCs show that small changes in both *d* and *h* play a profound role in the relative plastic contributions from grain boundary sliding and dislocation glide. The interplay of *d* and *h* leads to a very broad transition region from grain boundary sliding dominated flow, where the strength of the material is weak and insensitive to changes in *h*, to grain boundary dislocation emission and glide dominated flow, where the strength of the material is strong and sensitive to changes in *h*. The study of the fracture behavior of MNCs shows that cracks in Cu and Nb layers may exhibit different propagation paths and distances under the same external loading. Interfaces can improve the fracture resistance of the Nb layer in Cu/Nb MNCs by providing mobile dislocation sources to generate the plastic strain at the crack tip necessary for crack blunting. Increasing the layer thickness can further enhance the fracture resistance of both Cu and Nb layers, since the critical stress for activating dislocation motion decreases with increasing the layer thickness. A novel atomistic-informed interface-dislocation dynamics (I-DD) model has been developed to study Metal-Ceramic Nanolayered Composites (MCNCs) based on the key deformation process and microstructure features revealed by MD simulations. The I-DD predicted results match well with the prior experimental results where both yield stress and strain hardening rate increase as the layer thickness decreases. This I-DD model shows great potential in predicting and optimizing the mechanical properties of MNCs.

ACKNOWLEDGMENTS

First and foremost, I wish to express my sincere gratitude to my major advisor, Dr. Caizhi Zhou for his rigorous training, encouragement and guidance throughout my PhD study at Missouri University of Science and Technology.

I would also like to thank my other committee members, Dr. Matthew O'Keefe, Dr. David Van Aken, Dr. Mohsen Asle Zaeem and Dr. Xiaoping Du for their guidance and insightful suggestions.

Thanks also go to my wife Youqu Shen, my baby Lilian Huang, my parents and my friends Yunlu zhang, Zhiyuan wang, Lei Yan, Wei xiao and Yinan lin for their support during my study in Rolla.

TABLE OF CONTENTS

Page

PAPER

LIST OF ILLUSTRATIONS

Figure Page

SECTION

PAPER I

PAPER II

NOMENCLATURE

Symbol	Description
h	Layer thickness
d	Grain size
σ_{ys}	Yield strength
σ_o	Lattice fraction stress to slip
k	Hall-Petch slop
μ	Shear modulus
φ	Angle between slip plane and interphase plane
v	Poisson's ratio
b	Burgers vector
α	Dislocation core cutoff parameter
h_c	Critical layer thickness corresponding the strongest strength
δ_{ij}	Kronecker delta
E_i	Embeededd-atom method potential
F	Embedding function
γ_{ij}	Distance between atom i and j,
$\varphi_{\alpha\beta}$	Pair-wise potential function
P_β	Contribution to electron charge density.
P	Centro-symmetric parameter
$\vec{R}_i$	Vectors from atom i to one of its nearest neighbors
$\overrightarrow{dv}$	Relative distance vector

x_a	X coordinate for atom A
y_a	Y coordinate for atom A
z_a	Z coordinate for atom A
x_b	X coordinate for atom B
y_b	Y coordinate for atom B
z_b	Z coordinate for atom B
$\overrightarrow{Slip_v}$	Displacement vector
ε^{dis}	Plastic strain induce by dislocation slip
$\bar{n}_i$	Unit normal of the slip plane for the dislocation slipping over the atom *i*,
$\bar{l}$	Loading direction,
A	Unit area of atoms projected on the slip plane,
ϵ_{ijk}	Permutation tensor
κ	Curvature of dislocation line
B	Resistive matrix which determine the mobility of dislocation
α	Angle between tangent and burgers vector
n	Normal to the dislocation line vector t on the glide plane
B	Resistive matrix
V	Velocity of dislocation segment
f	Total force acting on dislocation segment
r_k	Displacement vector

Acronyms	Description
MNCS	Metallic Nanolayered Composites
MD	Molecular Dynamics
I-DD	Interface-Dislocation Dynamics
MCNCs	Metal-Ceramic Nanolayered Composites
PVD	Physical Vapor Deposition
ARB	Accumulated Roll Bonding
FCC	Face Centered Cubic
BCC	Body Centered Cubic
KS	Kurdjumov-Sachs
NW	Nishiyama-Wasserman
OR	Orientation Relationship
TEM	Transmission Electron Microscopy
IP	Interface Plane
CLS	Confined Layer Slip
NC	Nanocrystalline
GBs	Grain Boundaries
IFs	Interfaces
DFT	Density Functional Theory
LAMMPS	Large-scale-Atomic/Molecular Massively Parallel simulator
ps	Picosecond
cpus	central processing units
PS	Pair Separation Distance

EAM	Embedded-Atom Method
CSP	Centro-Symmetric Parameter
CNA	Common Neighbor Analysis
GBS	Grain Boundary Sliding
DXA	Dislocation Extraction Algorithm
3-D	Three-dimensional
DDD	Discrete Dislocation Dynamics
PDD	Parametric Dislocation Dynamics
FR	Frank-Read
NL	Nanolayered
SX	Single Crystalline
PX	Polycrystalline
NPT	Isobaric isothermal ensemble
GBE	Grain Boundary Dislocation Emission
CRSS	Critical resolve shear stress
SIF	Stress Intensity Factor
Cu	Copper
Nb	Niobium
Ni	Nickel
Al	Aluminum
TiN	Titanium Nitride

SECTION

1. INTRODUCTION

1.1. METALLIC NANOLAYERED COMPOSITES

Novel materials with better properties than the most advanced materials today are always desirable. Metallic Nanolayered Composites (MNCs) are one of the few nanostructured materials that exhibit a multitude of attractive structural and functional properties, including high strength, ductility, hardness, radiation resistance, fatigue resistance and good thermal stability [1-4]. Similar to the nanostructure bainite [5], MNCs have a plate-like microstructure and the scale of the microstructure achieved is very fine (layer thickness is below 40 nm). Very recently, advanced manufacturing methods have been employed to fabricate the MNCs in substantially larger sizes (above 10 millimeter), suitable for shaping them into macro-scale structures, enabling exploitation of their exceptional suite of properties in a broader range of applications [6,7].

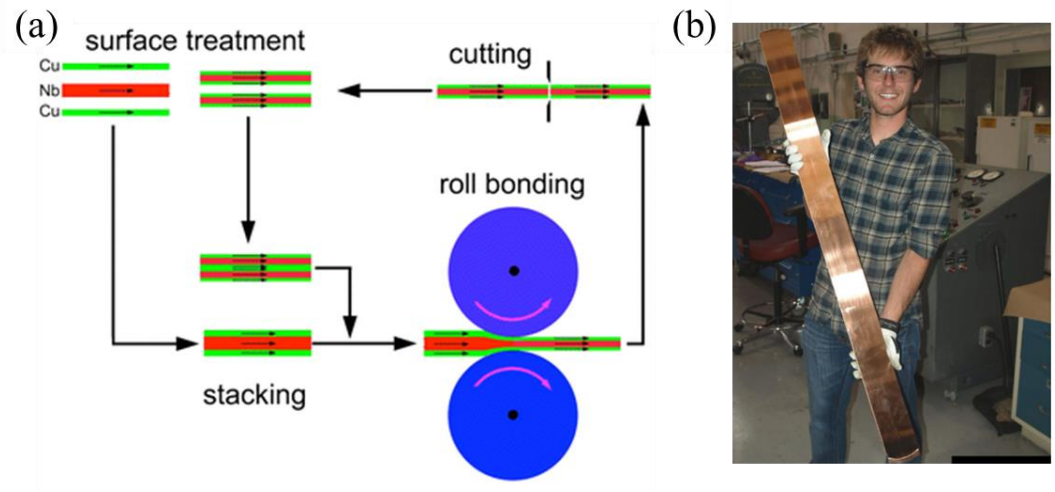

Figure 1.1. (a) Schematic of the ARB process for top–down synthesis of MNCs [8]. (b) Bulk Cu/NB MNCs produced by ARB process [9].

In general, MNCs can be produced by two methods: a Physical Vapor Deposition (PVD) technique and Accumulated Roll Bonding (ARB) processes [2,10,11]. Both methods can produce two-dimensional planar nanocomposites with a specific phase size down to the nanoscale. A PVD method utilizes a bottom-up process to generate a sample in the form of thin films. As shown in Figure 1.1, the ARB processes are achieved by repeatedly rolling, sectioning, stacking, bonding and rerolling and produces the sheet material in bulk form [8,9], which makes this method more commercially adaptable to production.

1.2. INTERPHASE BOUNDARIES OF MNCS

The mechanical properties of MNCs are significantly influenced by the interphase boundaries. Interphase boundaries can act as sinks, sources or the barrier for defects, e.g. dislocations and vacancies. There are two types of interphase boundaries in MNCs. One type of the interphase boundary exists when the two phases have the same crystallographic structure. A dislocation can transmit the interphases boundary from one phase to another phase by overcoming the high coherent stress in the interphases boundary since the slip system is exactly the same for the two phases and continues in this interphase boundary [12,13]. Cu/Ni MNCs contain these types of interphase boundaries. Both phases of Cu/Ni MNCs belong to the Face Centered Cubic (FCC) system and the lattice parameter for these two phases are close to each other (3.615 Angstrom and 3.52 Angstrom). Another type of the interphase boundary exists when the two phases have different crystal structures, e.g. the Cu/Nb MNCs where Nb is Body Centered Cubic (BCC). Interfacial misfit dislocations are needed to remove incompatibilities between two different slip systems [12,14]. A dislocation is difficult to transmit the interphase boundary since the slip system in each phase is discontinuous at the boundary. The two phases can adopt a classical Kurdjumov-

Sachs (KS) or a Nishiyama-Wasserman (NW) Orientation Relationship (OR) for MNCs with FCC and BCC systems in each layer, e.g. the Cu/Nb MNCs. As characterized by diffraction techniques and Transmission Electron Microscopy (TEM), Cu/Nb MNCs produced by the ARB processes generally adopt the {112} KS OR, while Cu/Nb MNCs produced by a PVD method generally adopt the {111} KS OR or the NW OR [15,16]. For a {112} KS OR, the interface plane (IP) is {112}fcc||{112}bcc and ⟨111⟩fcc||⟨110⟩bcc in-plane. For a {111} KS OR, the IP is {111}fcc||{110}bcc and ⟨112⟩fcc||⟨112⟩bcc in-plane. For a NW OR, the IP is {111}fcc||{110}bcc and ⟨110⟩fcc||⟨001⟩bcc in-plane.

1.3. MECHANICAL PROPERTIES OF MNCS

The layer thickness of MNCs plays a significant role in determining the deformation mechanism. The layer thickness size effect on the strength of the MNCs has been observed experimentally and computationally, and these results indicate that the deformation mechanism varies with different length scales [17,18]. Figure 1.2 illustrates the relationships between the layer thickness and deformation mechanisms. When the layer thickness varied from microns to hundreds of nanometers in region 3 (Figure 1.2), the strength of the MNCs can be predicted by a traditional Hall-Petch relationship [17]. This is because the spaces between the interfaces are large enough to accommodate the dislocation pile-up. Therefore, the interphase boundary works the same as a high angle grain boundary [18]. A Hall-Petch relationship states that as the grain size decreases, the yield strength increases. When it comes to the MNCs with the layer thickness in region 3, the yield strength is inversely proportional to the square root of the layer thickness (h).

$$\sigma_{ys} = \sigma_0 + kh^{-0.5} \tag{1.1}$$

where k is the Hall-Petch slop and σ_0 is the lattice fraction stress to slip.

The pile up of dislocations becomes more difficult as the layer thickness decreases below 100 nanometers. Therefore, a Hall-Petch relationship does not work. Instead, another mechanism commonly referred as Orowan bowing occurs. A threading dislocation with a hairpin configuration glides in a phase between two interphase boundaries and contributes most of the plasticity. The stress required to glide a threading dislocation can be defined as the critical stress.[19] A model called Confined Layer Slip (CLS) can be used to predict the critical stress [18].

$$\tau_{CLS} = \frac{\mu b \sin\varphi}{8\pi h}\left(\frac{4-\nu}{1-\nu}\right)\ln\frac{\alpha h}{b\sin\varphi} \tag{1.2}$$

where h is the film thickness, μ is the shear modulus, ν is the Poisson's ratio, φ is the angle between a slip plane and a interface plane, b is the Burgers vector, and α represent the dislocation core cutoff parameter (Low values of α imply a wide dislocation core). From this equation, the critical stress dependence on layer thickness is proportional to ln(h)/h.

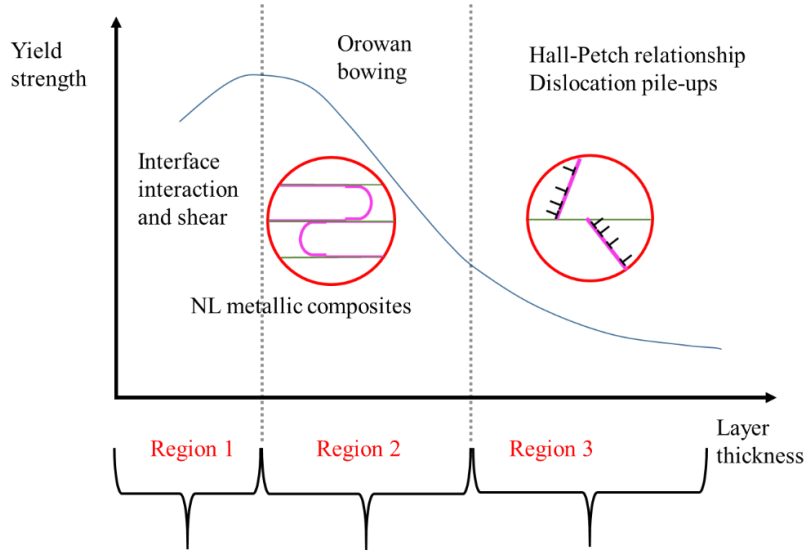

Figure 1.2. Schematic showing dependence of yield strength of MNCs on the individual layer thickness.

The CLS model may overestimates the yield stress as the layer thickness is reduced to few nanometers. Transmission of dislocations across the interphase boundary may also be possible. In addition, the interaction between interface misfit dislocations plays a significant role in determining the deformation behavior since the density of interphase boundary will become extremely large as a layer thickness down to a few nanometers is produced.

1.4. LITERATURE REVIEW AND MOTIVATION

A large number of studies over the past decade involving in-situ TEM, X-ray diffraction, atomic-scale modeling, and dislocation theory, have been devoted to understanding how interfaces affect dislocation motion in strained MNCs [14,20-27]. Many theories and atomistic simulations have shown that the interfaces can act as sources, sinks, barriers, and/or storage sites for dislocations and deformation twins.[14,22-24]

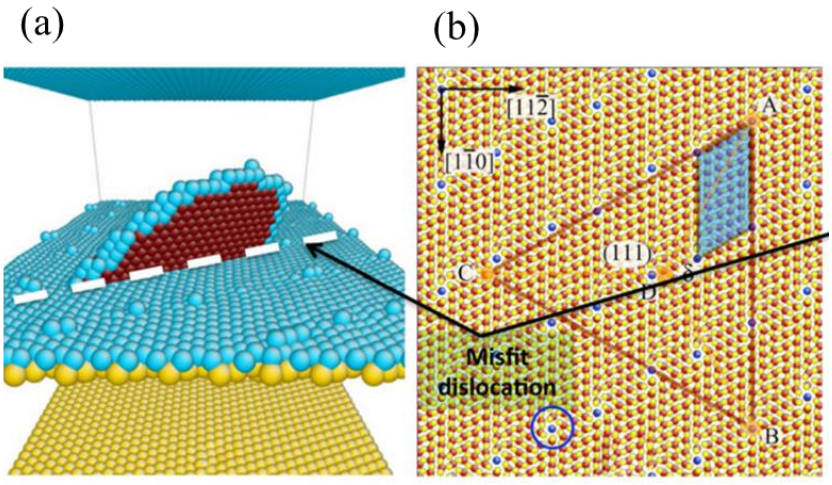

Figure 1.3. (a) Nucleation of a single Shockley partial dislocation loop when the bi-crystal model is subjected to in-plane tension. This loop was induced by stress concentrations in the interface generated around a misfit under the applied strain state, (b) plan view of the interface showing the intersection lines formed between three Cu {111} slip planes and the {111} plane of the interface.[8]

The interphase boundary types are associated with an interface formation energy and a low interface energy leads to a more stable interface. Fabrication methods, e.g. the PVD method and the ARB processes, can influence the interphase boundary type. An atomistic simulation indicated that the formation energy of {112} KS Cu/Nb interphase boundaries are about 850 mJ/m^2 and the formation energy of {111} KS Cu/Nb interphase boundaries are about 580 mJ/m^2 [28-30]. Both experimental and modeling work indicates that Cu/Nb interphase boundaries are weak and may be sheared easily because of the low shear strength relative to the layers [15]. Atomistic simulations show that the interface shear is associated with the interface type (e.g. {111} KS, {112} KS and NW) or the interface shape (e.g. flat and curved). A {111} KS Cu/Nb interface is relatively flat compared to a {112} KS Cu/Nb interface, which make it easier to shear [28,31]. The dislocation nucleation process as well as the relationship between dislocation nucleation and interface pattern in MNCs have been studied by many atomistic simulations as shown in Figure 1.3 [8,23]. A misfit dislocation in the interphase boundary would be nucleated into a layer when the resolved shear stress for dislocation slip system is exceeds a critical value [32-34]. A dislocation in the phase would tend to glide within the phase and deposits dislocations in the interphase boundary since the energy for a dislocation to transmit across the interface is high, [35].

In some experimental studies a limit value of the critical layer thickness, h_c, has been reported below which strength no longer increases but plateaus or drops with the decreasing of layer thickness [20,22,26,27]. Using dislocation theory, the highest strength of MNCs has been postulated to occur at the crossover from confined layer slip to slip transfer across the bi-phase boundaries [18]. Yet, whether or not a limiting h_c is found, the reported

sensitivity of MNCs strength to *h* can vary among studies on similar MNCs [6]. Much of the variability can be attributed to different choices of strength measures, either yield or peak strength in tension or compression, or indentation hardness, or to processing-induced variations in the microstructure, such as texture or the in-plane sizes of the grains *d* within the nanocrystalline (NC) layers [36]. It, therefore becomes apparent that understanding the role that interfaces, the interface boundaries density, and spacing play in affecting dislocation motion, and therefore strength, would help in rationalizing these results.

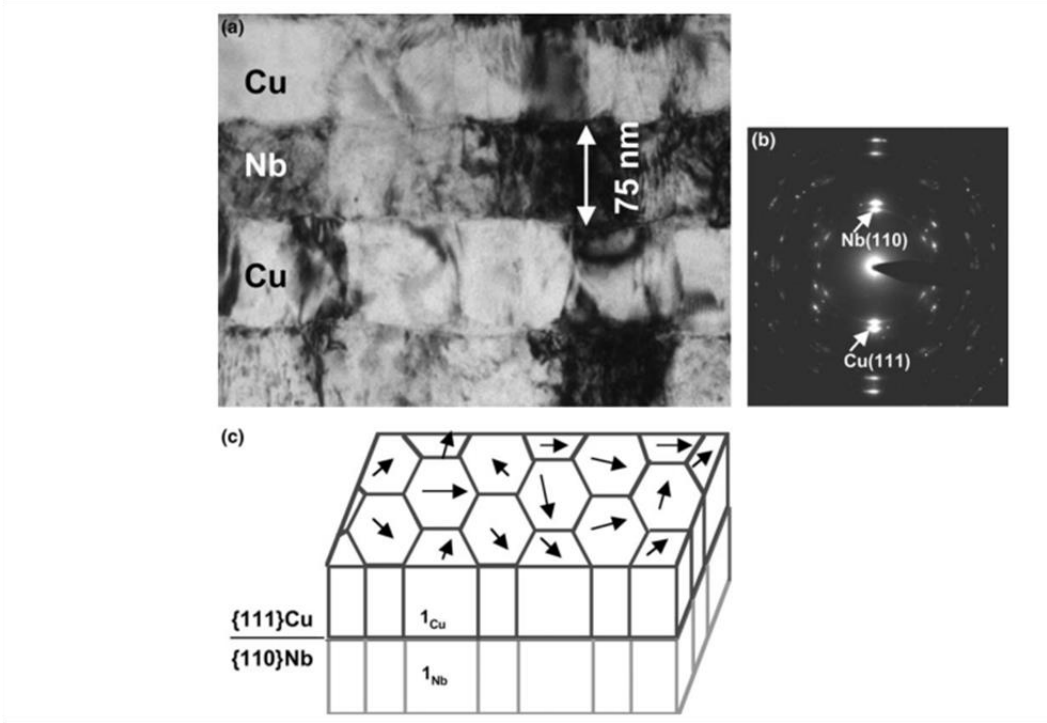

Figure 1.4. (a) Bright field TEM micrograph, (b) corresponding selected area diffraction pattern of a sputter-deposited 75 nm Cu/75 nm Nb MNCs, and (c) schematic illustration of the texture, with the arrows denoting the in-plane Kurdjumov–Sachs directions, 〈1 1 1〉 Nb// 〈1 1 0〉 Cu, for each of the columnar Cu/Nb grain pairs [2].

One prominent nanostructural feature that is missing in most studies is the nanocrystalline grain structure of the individual layers as shown in Figure 1.4. Two length

scales, therefore, should be used to describe nanocrystalline MNCs: *h* the mean distance between interfaces (IFs) and the grain size *d*, defined as the mean in-plane distance between adjacent Grain boundaries (GBs). Collecting knowledge gained from studies in either NC materials or MNCs indicates that both GBs and IFs would greatly affect the dynamics and kinetics of dislocations in strained materials. To date, few calculations or theories have been reported to understand the coupled effect of GBs and IFs on the deformation of MNCs. A majority of the Molecular Dynamics (MD) work that connects grain boundary affected dislocation motion, nanograin size, and strength pertain to single-phase nanocrystalline (NC) metals [36-39]. Most MNC modeling studies treat the layers as single crystalline and not as NC [14,20-22]. Recently, Zhu et al.[26,27] investigated size effects in polycrystalline MNCs by MD simulations and found that the micro-plasticity deformation can be dominated by several possible dislocation mechanisms, e.g. gliding of partial dislocation versus gliding of full dislocation. While both length scales *h* and *d* could be feasibly altered in manufacturing, and values for *h* and *d* needed to achieve the highest yield or flow strength are not known. Key questions need to be addressed: Which length scale, *h* or *d*, dominates and controls the peak strength or the onset of softening? Is it plausible to believe that the finest length scale, the one that is the closest in length scale to the dislocations, would be the one that controls strength behavior of the material? To date, there are no calculations or theories that consider the coupled roles in deformation to confirm or deny that the finest length scale would controls strength behavior of the material or any notion regarding the coupled effect of grain boundaries and interfaces on dislocation nucleation and motion.

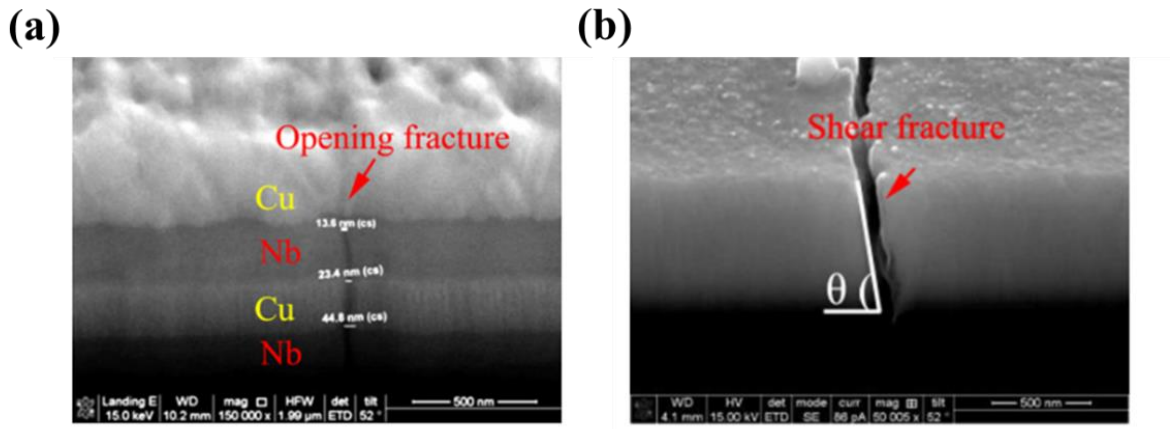

Figure 1.5. Two kind of fraction model found by Zhang at el. [42] with different layer thickness and layer thickness ratio. (a) Opening fracture model with larger layer thickness; (b) Shear fracture model with small layer thickness.

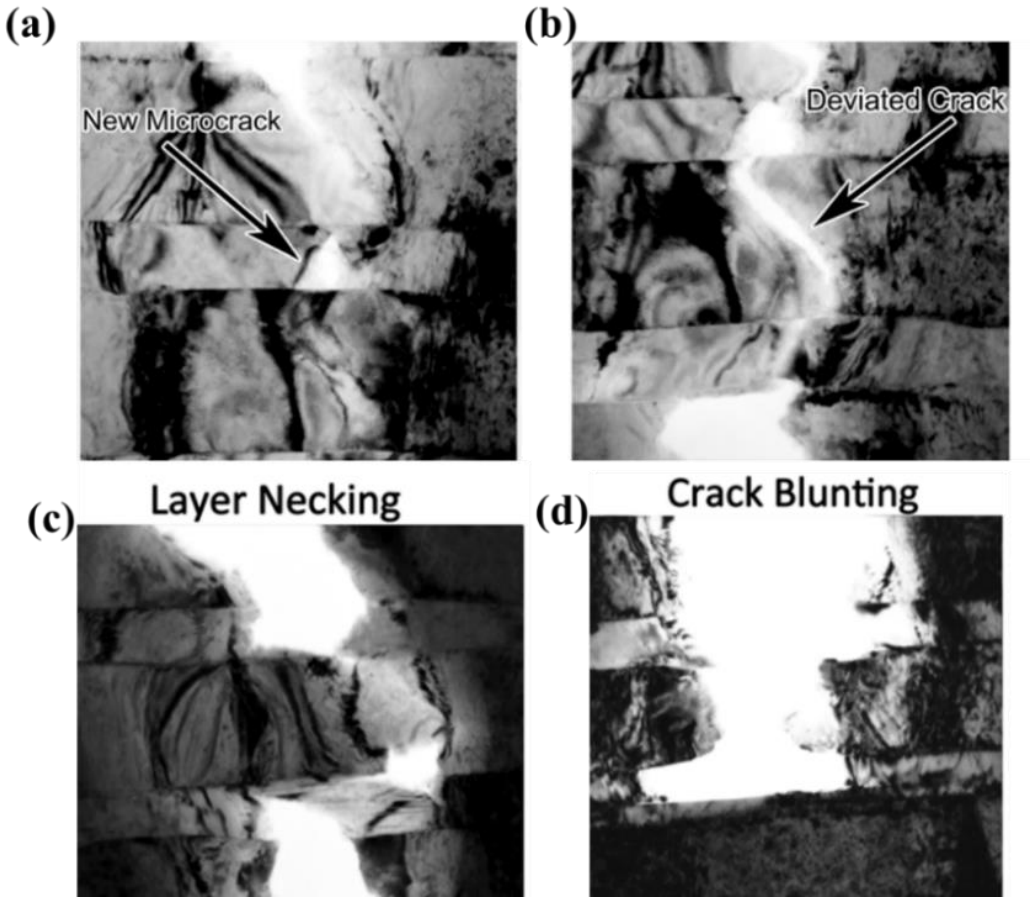

Figure 1.6. Four crack hindrance processes during crack propagation found by Hattar et al.[41]. (a) micro-void; (b) crack deviation: (c) layer necking; (d) crack blunting.

Another important mechanical property for MNCs is their ductility. The interfaces in MNCs not only influence the strength but also affect the ductility property and the fracture mechanism. To explore the fracture mechanisms in MNCs, Zhu et al. [40] examined the deformation zone ahead of the crack tip in the Cu/Ta MNCs and revealed a critical layer thickness, below which the fracture mode of the MNCs tends to be a shearing failure. Zhang et al. [42] studied the fracture behavior of Cu/Nb and Cu/Zr. Their experimental results demonstrated that as the layer thickness of the Cu layer decreased below 60 nm the fracture mode transitioned from brittle fracture (characterized by low ductility) to shear fracture as shown in Figure 1.5. Based on their experiment results, Zhang et al. claimed that the transition of fracture modes is dominated by the constraint of the soft Cu layer on the brittle Nb or Zr layer. Hattar et al. [41] demonstrated four fracture steps (crack deviation, layer necking, micro-void formation and crack blunting) during the crack propagation in Cu/Nb by using an in-situ transmission electron microscopy straining test as shown in Figure 1.6. Liang et al. [43] performed tensile tests on Cu/Ni MNCs and revealed a transition of fracture modes from necking-inhibited brittle mode to necking-delayed ductile mode as the Ni layer thickness decrease from 90 to 40 nm. However, it is still unclear how the interface in MNCs affects the fracture mechanism of MNCs and how the crack interacts with the interface under external loading.

1.5. DISSERTATION OBJECTIVES

An atomistic simulations can reveal the underling atomic scale deformation processes in metallic systems and then shed light onto the deformation and failure mechanisms in nanostructured materials. The primary objective of this research is to use the atomistic simulations to study the effect of the interface, the layer thickness and the

layer grain size on the mechanical responses of MNCs. Firstly, MD simulations are applied to study the deformation of Cu/Nb MNCs and explore which length scale, the layer thickness or the grain size, dominates and controls the peak strength or the onset of softening and how they influence the strength. Secondly, MD simulations are applied to explore the fracture behavior of Cu/Nb MNCs and study effects of the interface, the layer thickness and grain boundaries.

The Three-Dimensional (3-D) Discrete Dislocation Dynamics (DDD) model is used for exploring the plastic deformation of metallic systems at both nano and micro-scales [66-74]. It should be noted that the 3-D DDD model has not yet been applied to the study of the mechanical response of nanolayered composites. Finally, a novel atomistic-informed interface-dislocation dynamics (I-DD) model is developed to study the nanolayered composites.

2. MOLECULAR DYNAMICS FUNDAMENTALS

2.1. INTRODUCTION OF MOLECULAR DYNAMICS

Atomistic modeling of materials can be performed by either Density Functional Theory (DFT) or by Molecular Dynamics (MD). A DFT model is preferred when length scales are less than 10 nm whereas an MD is used for predicting material behavior on length scales that range from 1-2 angstroms to 100 nm. The MD method is useful for studying deformation of both crystalline and non-crystalline materials. For crystalline materials, as will be presented here, the MD is used to model dislocation nucleation, multiplication, and interaction with grain boundaries and other dislocations during deformation. An MD model consists of a three-dimensional space with a coordinate system where atoms are located with local symmetry describing a specific crystal structure at absolute zero temperature, e.g. Face Centered Cubic (FCC), Body Centered Cubic (BCC), etc. This space is often referred to as the simulation box. An empirical atomic potential function is then assigned to each atom as part of the pre-processing of the MD model. Initial boundary conditions are applied to the model to create surfaces, grain boundaries, interphase boundaries and periodic boundaries to establish crystalline continuity. Appropriate temperatures and pressures are selected, and the MD model recalculates the position of each atom prior to the start of a simulation.

An MD simulation of deformation is performed by applying displacements to a plane of boundary atoms. A strain rate is established by the imposed displacement and the calculation time step, which is 10^{-15} s. A typical value for the strain rate is 10^{8} s^{-1}. For example, the total number of calculation steps will be on the order of 200,000 if a 2% elongation is imposed upon the simulation box. A calculation step determines the forces

applied to each atom using both the applied displacement and the internal forces generated by neighboring atoms within a 5 nm distance. These forces result in a velocity vector that can be used to calculate the new position of each atom. In addition to the coordinate position of each atom the stress state, energy, and temperature of the system are determined at each time step. Post processing at the end of the simulation will include determining the coordination of the atoms and their neighboring atoms to identify local crystal type e.g. (FCC or BCC) and observe both planar and linear defect types (stacking faults and dislocations). The main advantage of the MD method is that it can provide the location of each atom at any time during the simulation. Thus, microstructural evolution at the atomistic scale can be clearly observed with the help of visualization software such as Ovito. [44]

Two key challenges remain for the MD computational method. First, the dimensions of the simulation box are currently limited to about 100 nm using 128 cpus (central processing units) with a calculation time of one week. Greater computing power is required when the microstructural scale is larger than 100 nm, e.g. a polycrystalline microstructure with a grain size larger than 100nm. The second challenge is the time step, which is 10^{-15} s, which imposes a strain rate at least 10,000 times faster than in experimental studies.

There are many codes which can be used to do the MD simulation. In this study, the LAMMPS code is used. LAMMPS is an acronym for Large-scale-Atomic/Molecular Massively Parallel simulator. It is a classical molecular dynamics code and the code can be run on a single processor or in parallel using a multiple cpu cluster [45].

2.2. ENSEMBLE, BOUNDARY CONDITION AND LOADING METHOD

A statistical ensemble is a method used to integrate the system (all atoms in the simulation box), for example, the ensemble of Newton's equations of motion can make the system have a constant-energy surface. In MD simulations, three ensembles are commonly used: a microcanonical ensemble, a canonical ensemble and an isothermal-isobaric ensemble. In the microcanonical ensemble, the volume and the total energy in the system are held constant. In the canonical ensemble, the total volume and the temperature in the system are held constant. In isothermal-isobaric ensemble, the temperature and the pressure in the system are held constant. During MD simulations, the isothermal-isobaric ensemble can control the temperature by a Nose-Hoover algorithm which connects a system to a heat bath and control the pressure by altering the simulation box size. The isothermal-isobaric ensemble is preferred by many MD works as it can mimic the experimental temperature and pressure.

In MD simulations, three boundary condition are commonly used: a free surface boundary condition, a fixed boundary condition and a periodic boundary condition. The free surface boundary condition treats the space outside the surface layer of atoms as the vacuum. The fixed boundary condition treats the surface layer of atoms as a "rigid plane" which is immobile. Finally, the periodic boundary condition connects the atoms from one side to the other sides, making the dimension infinite. As shown in Figure 2.1, a free surface boundary condition is applied in the y direction and a periodic boundary condition is applied in x direction. Copying the central group of atoms within the simulation box to the left side or the right side and atoms in the boundary region still belong perfectly to the layer

crystal structure. The periodic boundary condition is the most common boundary condition used in MD simulations as it can reduce the total number of atoms in the model.

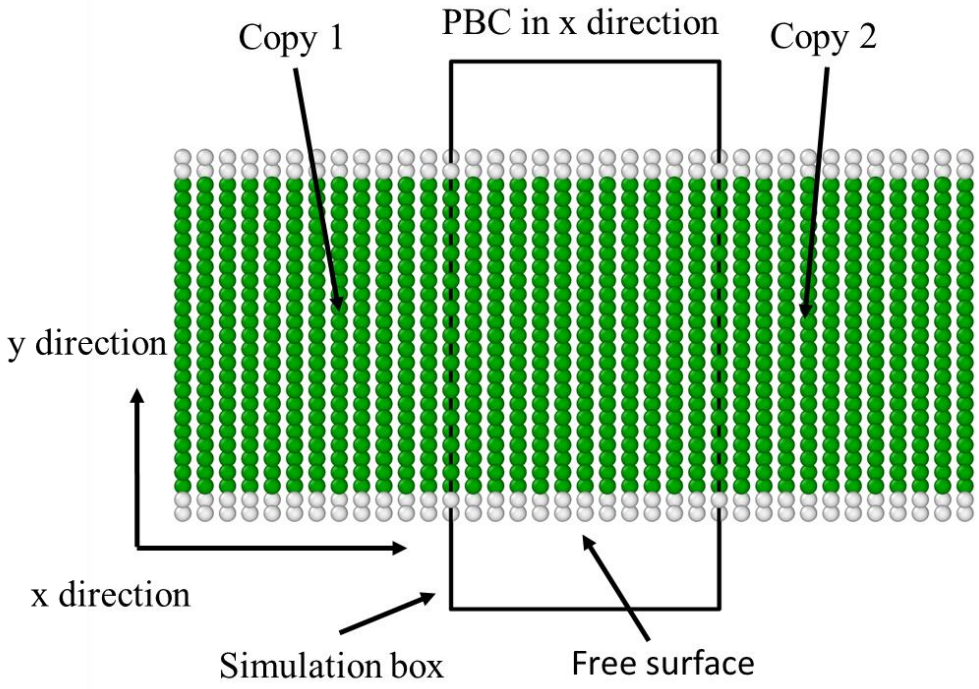

Figure 2.1. Two-dimensional periodic boundary condition. The central atoms within the simulation box is the original one which is surrounded by 2 exact copies of itself on left and right side.

In MD simulations, the deformation mechanisms can be explored by applying a strain to a sample, and two methods are commonly used to apply a strain. Firstly, a strain is applied by altering the size of the simulation box at each time step. The coordinate system of atoms would be reallocated if the simulation box enlarges or shrinks at one dimension or multi-dimensions. The first method only works for the periodic boundary condition. The second method utilizes the fixed boundary condition. By giving the outside fixed layer of atoms a displacement and allowing inside atoms to relax at a given time, e.g. 1

picosecond (ps), a strain (equal to the displacement divided the initial length of the simulation in displacement direction) would be applied in the sample.

2.3. THE INTERACTIVE POTENTIAL

MD simulations rely on interatomic potential to predict the behavior of atoms, so the accuracy of a potential is critically important as it determines the material's properties, e.g. a stacking fault energy, the Young's modulus. A simulation with a realistic potential requires too much computational resource, e.g. thousands of cpus and thousands of hours. To complete a simulation in a reasonable amount of time, empirical interaction potentials, e.g. Lennard-Jones potentials, Tersoff potentials, Morse potentials and Embedded-Atom Method (EAM) potentials have been developed and they have proven to be very efficient in evaluating a systems up to ten million atoms [46-49]. In general, the simple pairwise potentials, e.g. Lennard-Jones potentials, are not as good as the many-body embedding functional potentials, e.g. EAM potentials, because of some inherent limitations such as the inability to describe all elastic constants for cubic metals. The bond strength and local environment of an atom are considered in the EAM potential [49]. Ziegenhain et al. compared the mechanical properties of Cu predicted by using a pair potential and an EAM potential and found that the pair potential cannot model the elastic anisotropy of cubic crystals and underestimated the stable stacking fault energy [50]. Many previous MD works utilized the EAM potentials and provided significant findings such as the characterizing of the softening in nanocrystalline metals at small grain sizes [75]. Due to the efficiency of the many-body embedding potential, the EAM potential was selected to do the MD simulation. The equation for EAM potential is given by [51]

$$E_i = F_a\left(\sum_{i\neq j} P_\beta\left(\gamma_{ij}\right)\right) + 0.5\sum_{i\neq j}\varphi_{\alpha\beta}\left(\gamma_{ij}\right) \quad (2.1)$$

where F is an embedding function, γ_{ij} is the distance between atom i and j, $\varphi_{\alpha\beta}$ is the pair-wise potential function and P_{β} is the contribution to electron charge density.

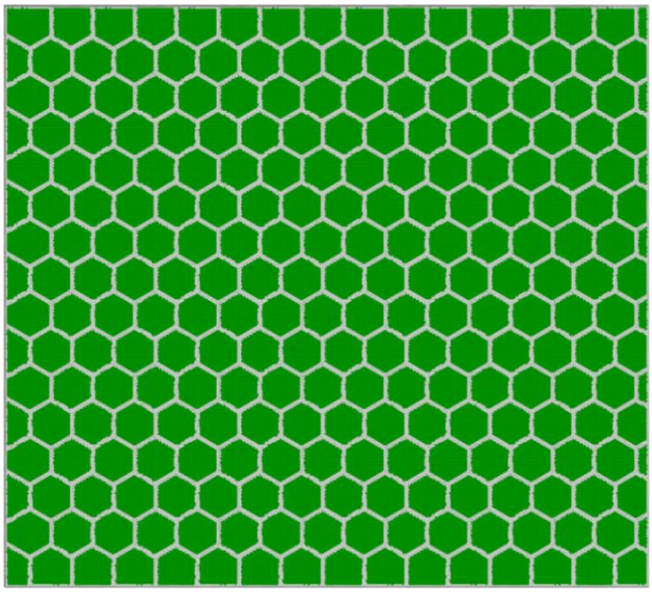

Figure 2.2. Polycrystalline model generated by the 2D Voronoi algorithm

2.4. PRE-PROCESSING: STRUCTURE GENERATION

Some of the metallic samples in this study are polycrystalline, e.g. Cu/Nb MNCs. In these samples, each layer has columnar and hexagonal shaped grains with different crystallographic orientations. A modified Voronoi method is used to create the polycrystalline metallic samples [52]. The layers in this study are columnar polycrystalline, therefore, only two-dimension distance were considered. For the Voronoi method, a coordinate system for the seed of each grain should be defined. The seeds represent the center of each grain. The distance between seeds should be larger than the grain's radius, which make the grain structure reasonable. The seeds are distributed randomly such that an average d is obtain and each grain has a hexagonal shape. In order to make sure each grain has a regular hexagonal shape as show in Figure 2.2, the coordinate systems for seeds

are defined specifically. Then the crystallographic orientations for different grains should be specified. Two different grains which share a grain boundary are selected to have a relatively different crystallographic orientations, otherwise the grain boundary between the two grains is unstable. A transformation matrix can be used to set the crystallographic orientation for each grain. Finally, coordinate systems for all atoms can be specified based on the coordinate systems for each seed and the transformation matrixes for each grain. An example of columnar polycrystalline sample generated by a 2D Voronoi method is shown in Figure 2.2 and a corresponding FORTRAN code is shown in APPENDIX A.

2.5. POST-PROCESSING: ANALYTICAL METHOD AND VISUALIZATION

Post-processing is needed to better understand the evolution of the microstructure for a simulation, e.g. a uniaxial compression. In general, the original information outputted from a MD simulation only contains the three-dimension coordinates for each atom. A post-processing can provide some independent parameters, e.g. a Centro-Symmetric Parameter (CSP)[53] and a Common Neighbor Analysis (CNA)[54] parameter. With the help of a visualization software, different types of defects, e.g. the grain boundary, the twin boundary, the interphase boundary, the stacking fault and the dislocation core, can be easily observed and identified. The CSP and the CNA parameters are commonly used in the post-processing of MD simulation. CSP is computed by:

$$P = \sum_{i=1}^{N/2} |\vec{R}_i + \vec{R}_{i+N/2}| \tag{2.2}$$

where $\vec{R}_i$ are vectors from atom i to one of its nearest neighbors and N is the number of nearest neighbors, for the FCC structure, N equal to 12 and for the BCC structure, N equal

to 8. A CSP is used to characterize the degree of inversion symmetry breaking in each atoms' local environment.

A post-processing can also be used to identify different plastic deformations and calculate the plastic contribution from different activities, e.g. dislocation gliding and grain boundary sliding. The first step involves identifying the nearest neighbors for each atom before the deformation and the second step involves calculating the displacement vectors after the deformation. A displacement vector is a measure of the relative motion between nearest neighbor pairs of atoms compared to its initial value. Specifically, as show in Figure 2.3, before the deformation, an atom B is one of the nearest neighbors of an atom A and their relative distance vector can be calculated by:

$$\overrightarrow{dv^{intial}} = (x_a^i - x_b^i, y_a^i - y_b^i, z_a^i - z_b^i) \tag{2.3}$$

where x_a^i is the x coordinate for atom A, y_a^i is the y coordinate for atom A, z_a^i is the z coordinate for atom A, x_b^i is the x coordinate for atom B, y_b^i is the y coordinate for atom B, z_b^i is the z coordinate for atom B. After the deformation, a new relative distance vector can be recalculated by:

$$\overrightarrow{dv^{deform}} = (x_a^d - x_b^d, y_a^d - y_b^d, z_a^d - z_b^d) \tag{2.4}$$

Then, the displacement vector can be calculated by:

$$\overrightarrow{slip_v} = \overrightarrow{dv^{deform}} - \overrightarrow{dv^{intial}} \tag{2.5}$$

If no slip activity happens for a pair of neighbor atoms, e.g. atom B and atom D, the displacement vector would be close to zero. If a slip activity happens for a pair of neighbor atoms, e.g. atom B and atom A, the displacement vector would be the slip vector. The magnitude of the vector can specify the slip activity, e.g. full dislocation slips, partial dislocation slips.

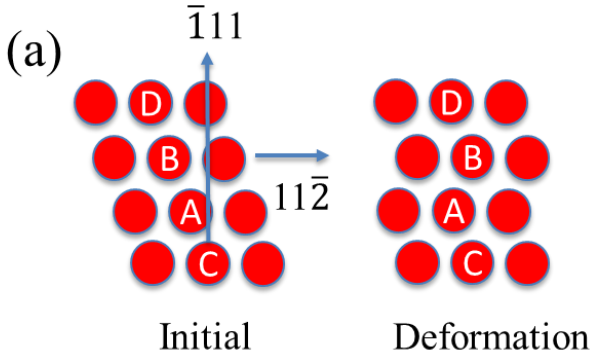

Figure 2.3. Example slip activity happens for atom B relative to atom A

After slip vectors are determined, the relative amounts plastic contribution from the partial dislocation gliding, the full dislocation gliding, and the grain-boundary-mediated deformation can be determined. The first step involves identifying the atoms in the grain interiors using the CSP or CNA parameter. Then the amount of strain contributed by partial or full dislocation glide can be calculated by summing the strain induced by all atoms displaced by dislocation motion, as follows:

$$\varepsilon^{dis} = \sum_i^N \frac{A}{V} \times (\bar{l} \cdot \bar{b}_i) \times (\bar{l} \cdot \bar{n}_i) \tag{2.6}$$

where $\bar{b}_i$ is the Burgers vector of the dislocation slipping over the atom i, $\bar{n}_i$ is the unit normal of the slip plane for the dislocation slipping over the atom i, $\bar{l}$ is the loading direction, A is the unit area of atoms projected on the slip plane, V is the volume of the simulation box, and N is the total number of slipped atoms. All other atomic shifts not associated with dislocation glide are attributed to grain boundary deformation, such as grain boundary sliding and diffusion

Another important post-processing method is the Dislocation Extraction Algorithm (DXA) which was developed by Kelchner et al [55]. The fundamental concept underlying the

DXA is the Burgers circuit construction [56]. It is very useful to get the dislocation information which includes the dislocation density and dislocation type. This method is integrated into the Ovito software. By this method, dislocation lines can be clearly observed in the microstructure as shown in Figure 2.4.

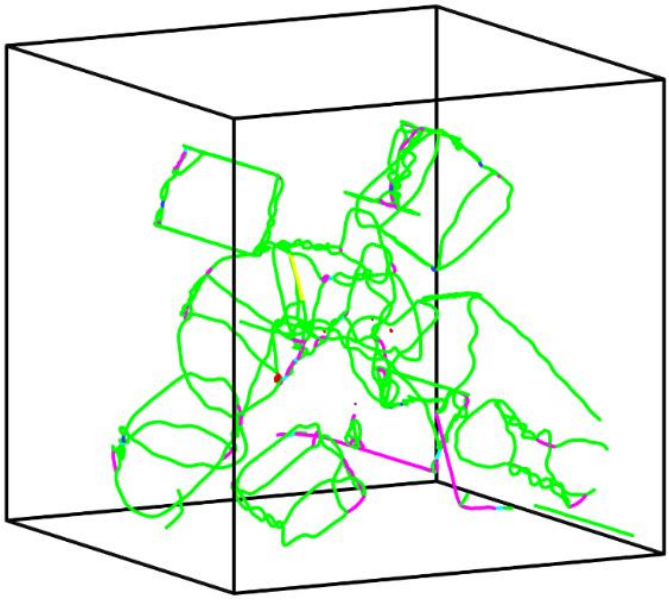

Figure 2.4. Dislocation structure in MD simulation generated by the Dislocation Extraction Algorithm (DXA) method [55].

3. DISLOCATION DYNAMICS FUNDAMENTALS

3.1. INTRODUCTION OF DISLOCATION DYNAMICS

Dislocation Dynamics (DD) is a computational modeling method that is preferred when the scale ranges from 100 nm to 10,000 nm. DD simulations simplify the modeling by only considering the dislocation core volume only, which increases the calculation efficiency and makes them capable of handling much larger volumes than the MD simulations. Although DD simulations consider only the behavior of dislocations, they can provide valuable predictions because the slip of dislocations is considered the primary plastic deformation mechanism in metallic materials. In Three-Dimensional (3-D) Discrete Dislocation Dynamics (DDD), dislocations are represented as line defects and divided into straight or curved segments [57-64]. The most advanced 3-D DDD code includes various dislocation–based mechanisms, e.g. the dislocation interaction, the dislocation annihilation and the dislocation cross-slip. A 3-D DDD model is a powerful tool for exploring the plastic deformation of metallic systems. For the studies on MNCs, a 3-D DDD model can mimic the dislocation gliding within a small layer. In this study, a Parametric Dislocation Dynamics (PDD) developed by Ghoniem et al [64] is used.

3.2. STRESS AND EQUATION OF MOTION

To describe the behaviors of dislocation during the 3-D DDD simulation, the force acting on the dislocation and the equation motion are important factors. The stress field tensor for a dislocation segment can be obtained by [64]:

$$\sigma_{ij} = \frac{\mu b}{4\pi} \oint [\frac{1}{2} R_{,mpp} \left(\epsilon_{jmm} dl_i + \epsilon_{imn} dl_j\right) + \frac{1}{1-\nu} \epsilon_{kmn} (R_{,ijm} - \delta_{ij} R_{,ppm}) dl_k \quad (3.1)$$

where b is the burger vector and ϵ_{ijk} is the permutation tensor, μ is the elastic isotropic medium, $\delta_{ij}$is the Kronecker delta, v is the Poisson ratio and l is the line direction vector.

A self-force of a dislocation is another important force. In brief, since the dislocation is a line defect, the self-force can be thought of as the line tension. The force direction is directed to in the center of curvature of the dislocation loop. The formulation of the self-force use in this studies is developed by Gavazza and given below [64]:

$$\frac{F}{L} = \frac{\partial \frac{U}{L}}{\partial r} = -\kappa[E(\alpha) + E''(\alpha)\ln\left(\frac{8}{\varphi\kappa}\right) + \mu b^2[\kappa\left(\frac{21+\cos\alpha^2}{64\pi}\right) + \bar{\kappa}\left(\frac{2\cos\alpha^2-1}{2\pi}\right)]n \qquad (3.2)$$

where κ is the curvature, φ equals to the half of the magnitude of the burger vector, α is the angle between tangent and the burgers vector, n is the normal to the dislocation line vector t on the glide plane. The equation of motion is given by:

$$\oint_C (f_k^t(t) - B_{\alpha k} V_\alpha)\, \delta r_k |ds| = 0 \qquad (3.3)$$

where B is the resistive matrix which determine the mobility of dislocation, V is the velocity, r_k is a displacement vector and f is the total force acting on the dislocation. The total force is composed of the self-force, osmotic force [63] and the Peach-Koehler forces.

3.3. SIMULATION PROCEDURE AND FLOW CHART

The simulation methodology for a 3-D DDD simulation is illustrated in Figure 3.1. To start, initial dislocation structures, e.g. the dislocation loops and the Frank-Read (FR) sources, are randomly put in the simulation box and their burger vectors are specified. Material's properties such as the elastic modulus, a Poisson ratio, a lattice constant and a dislocation mobility are defined. During the simulation, the velocity of a dislocation segment can be calculated by solving the equation (3.8). Then the new position of each node can be determined according the velocity and the time step, e.g. 0.1 ps. After that,

short-range reactions such as the dislocation annihilation, the formation of dislocation junction and the cross-slip of dislocation are considered. The information such as the stress and the dislocation density can be output at the end of each step. Finally, the simulation enter to the next step and the cycle is built.

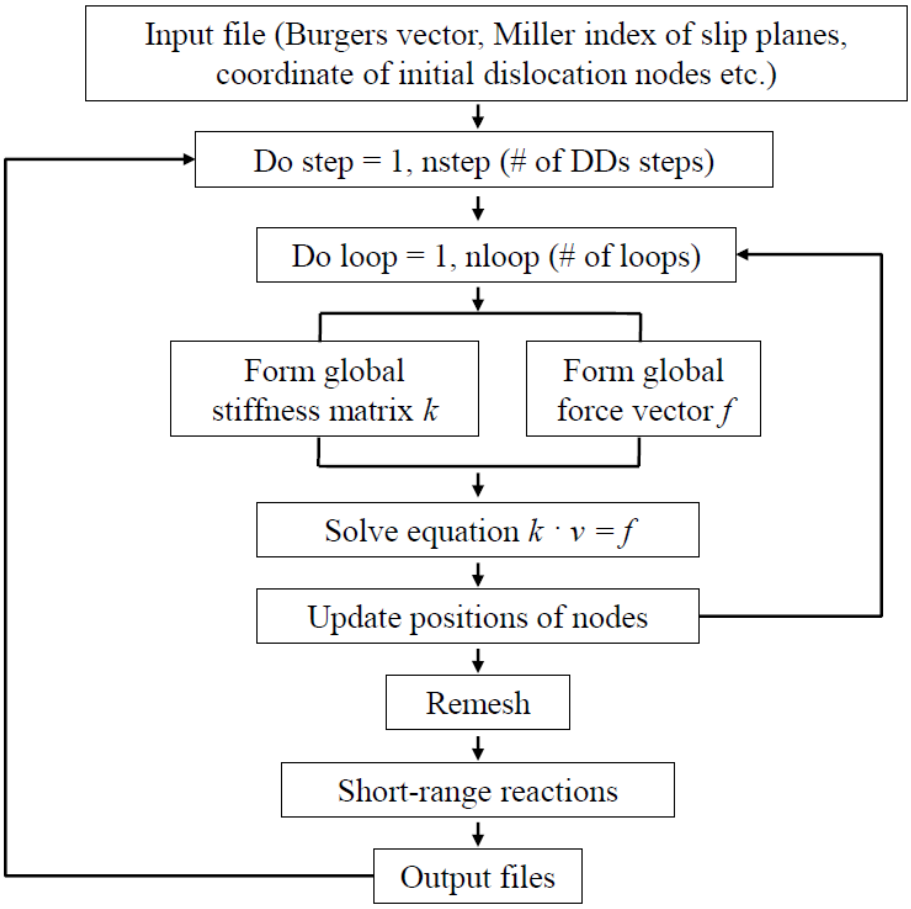

Figure 3.1. The flow chart of 3D-DDD simulation [65].

PAPER

I. NANOGRAIN SIZE EFFECTS ON THE STRENGTH OF BIPHASE NANOLAYERED COMPOSITES

Sixie Huang[1], Irene J. Beyerlein[2] and Caizhi Zhou[1,*]

[1] Department of Materials Science and Engineering, Missouri University of Science and Technology, Rolla, MO 65409, USA
[2] Department of Mechanical Engineering, Materials Department, University of California at Santa Barbara, Santa Barbara 93106, USA

Published in Scientific Reports, Volume 7: 11251, 2017

ABSTRACT

In this work, we employ atomic-scale simulation to uncover the interface-driven mechanisms governing the deformation response of nanoscale, layered composites. Two internal boundaries persist in these materials, the interlayer crystalline boundaries and intralayer biphase interfaces, and both have nanoscale dimensions. These internal surfaces are known to control the activation and motion of dislocations, and despite the fact that most of these materials bear both types of interfaces, the competing effects of their intralayer spacing (grain size, *d*) and intralayer biphase spacing (layer thickness, *h*), on first yield and peak strength have yet to be clarified. From our calculations, we find that the first defect event, signifying yield, is controlled by *d*, and not *h*. For the finest *d*, yield is defined by grain boundary sliding whereas for the remaining nanoscale range of *d*, it is determined by grain boundary source activation. Small changes in both *d* and *h* play a profound role in the relative contributions of grain boundary sliding and dislocation glide. The interplay of two internal sizes leads to a very broad transition region from grain boundary sliding dominated flow, where the material is weak and insensitive to changes in *h*, to grain

boundary dislocation emission and glide dominated flow, where the material is strong and sensitive to changes in *h*. Such a rich set of states and size effects are not seen in idealized materials with one of these internal surfaces removed. These findings provide some insight into how changes in *h* and *d* resulting from different synthesis processes can affect the strength of nanolayered materials.

Keywords: nanograin size, layer thickness, nanolayered composites, strengths

1. INTRODUCTION

Two-phase nanolayered (NL) metallic composites are one of the few nanostructured materials that uniquely exhibit a multitude of attractive structural and functional properties, ranging from high strength, ductility, hardness, radiation resistance, to thermal stability [1-4]. Very recently, advanced manufacturing methods have been employed to successfully make NL materials in bulk, that is, in sizes suitable for large structures. Scaling up in this way enables exploitation of their exceptional suite of properties in a much broader range of applications than thought possible [5,6].

NL composites are comprised of alternating layers of two metal phases, which individually are less than 100 nm. Usually one metallic nanocrystal spans an individual layer thickness *h*, joining from one bimetal interface to the other. Many studies on the strength of these materials find that decreasing *h* can strengthen the material, particularly when *h* lies in the nanoscale range, from 100 nm to 10 nm. It is believed that the nanoscale dimensions affect the selection of deformation mechanisms, such as dislocation glide and sliding along the interfaces or grain boundaries, which determine material strength, differently than in coarser dimensions and this nanoscale alteration grows as *h* decreases.

The dislocation core itself has nanoscale grain size dimensions, and thus, the movement of just one dislocation within a crystal, for instance, can have a noticeable impact on the strength of the entire NL composite. However, how *h* affects dislocation motion (including production and annihilation) needs to be better understood in order to identify the relation between *h* and the strength of NL composites.

A large number of studies over the past decade, involving in-situ TEM, diffraction, atomic-scale modeling, and dislocation theory, have been devoted to understanding how interfaces affect dislocation motion in strained nanolayered materials [7-15]. Many theories and MD simulations have shown that interfaces can act as sources, sinks, barriers, and/or storage sites for dislocations and deformation twins [9-12]. Li et al. revealed that interfaces in bimetal NL composites can provide the high diffusivity and vacancy concentration for promoting dislocation climb at room temperature. [16]. In some experimental studies, a limit value of the critical layer thickness, h_c, has been reported, below which strength no longer increases but plateaus or drops. Using dislocation theory, the strongest value of h_c has been postulated to occur at the crossover from confined layer slip to slip transfer across the bi-phase boundaries [17]. Yet, whether or not a limit h_c is found, the reported sensitivity of NL strength to *h* can vary among studies on similar NL materials [18] Much of the variability can be attributed to different choices of strength measures, either yield or peak strength in tension or compression, or indentation hardness, or to processing-induced variations in the microstructure, such as texture or the in-plane sizes of the grains *d* within the nanocrystalline (NC) layers [19]. It, therefore, becomes apparent that understanding role that interfaces and their densities and spacing play in affecting dislocation motion, and therefore strength, would help in rationalizing these results.

One prominent nanostructural feature that is missing in most studies is the nanocrystalline grain structure of the individual layers. Two length scales, therefore, should be used to describe NC NL composites: *h* the mean distance between interfaces (IFs) and the grain size *d*, the mean in-plane distance between adjacent GBs. Collecting knowledge gained from studies in either NC materials or NL nanocomposites indicates that both GBs and IFs would greatly affect the dynamics and kinetics of dislocations in strained materials. To date, not many studies involving calculations or theories have been carried out to understand the coupled effect of GBs and IFs on the deformation of NL composites. A majority of the MD work that connects grain boundary affected dislocation motion, nanograin size, and strength pertain to single-phase nanocrystalline (NC) metals [19-22]. Most NL modeling studies treat the layers as single crystalline and not as NC [7-10]. Recently, Zhu et al.[14,15] investigated size effects in nanolayerd polycrystalline metallic multilayers by MD simulations and found that the micro-plasticity deformation can be dominated by several possible dislocation mechanisms. While both length scales *h* and *d* could be feasibly altered in manufacturing, the values for *h* and *d* needed to achieve the highest yield or flow strength are not known. A key question then arises: which length scale, *h* or *d*, dominates and controls the peak strength or the onset of softening? Is it plausible to believe that the finest length scale, the one that is the closest in length scale to the dislocations, would be the one that controls strength of the material? To date, there are no calculations or theories that consider the coupled roles in deformation to confirm or deny this or any notion regarding the coupled effect of grain boundaries and interfaces on dislocation nucleation and motion.

In this article, we use MD simulation to explore the coupled effects of *h* and *d* on the yield and flow strength of NC NL composites. We apply the study to a Cu/Nb

nanolaminate with a nanostructure of one made by physical vapor deposition (PVD). We show that the strongest microstructural length scales do not correspond to the one with the finest dimension in both *h* and *d.* The grain size *d* affects the sensitivity of strength to reductions in layer thickness *h* increasing as *d* decreases. Once the material is deforming plastically, the flow stress is governed by the relative contributions of grain boundary-driven dislocation emission and grain boundary sliding. Although both are related to the grain boundaries, both *d* and *h* are found to govern the relative contributions of these two mechanisms. Analysis of the relative contributions of different grain boundary mechanisms (dislocation emission and subsequent slip vs. grain boundary sliding) explain that decreasing *d* can result in higher contributions of grain boundary sliding, a weaker composite, and reduced strength improvements with decreasing *h.* These results reveal that understanding the strength of nanostructured materials involves considering both *d* and *h*.

2. MATERIAL AND NANOSTRUCTURE

MD simulations of Cu/Nb multilayers were performed with the Large-scale Atomic/Molecular Massively Parallel simulator (LAMMPS) code [23]. Figure 1(a) shows the simulation cell for the polycrystalline (PX) NL Cu/Nb composites. Periodic boundary conditions have been applied to all three directions of this cell. The forces between Cu-Cu, Nb-Nb and Cu-Nb atoms were calculated by the interatomic potential [2,24,25] based on the Embedded Atom Method (EAM) [26]. This potential has been used previously in several studies on defect nucleation, formation, interactions, and propagation and replicates key defect properties, such as the energy of the stacking faults created by gliding partial dislocations [8,10-12].

Each layer is composed of four grains, and four Cu/Nb grain pairs connect across the interface. These hexagonal columnar grains were created by the Voronoi tessellation method [27]. To match the microstructure common for Cu/Nb composites synthesized via physical vapor deposition, the crystallographic orientation between each pair of Cu/Nb grains was made to follow the Kurdjumov-Sachs (KS) orientation relationship [28], meaning the directions in Cu and Nb for three axes are such that [1,1,0]Cu||[1,1,1]Nb are aligned in the X-axis, [1,1,2]Cu||[1,1,2]Nb in the Y-axis and [1,1,1]Cu||[1,1,0]Nb in the Z-axis. To create the nanograined sample, we fixed one pair of grains as the initial crystallographic orientation and rotated the other three pairs of Cu/Nb grains by 30°, 60° and 90° degree along the Z-axis. Consequently, grain boundaries were created in each layer while maintaining the KS orientation relationship for each pair of Cu/Nb grains.

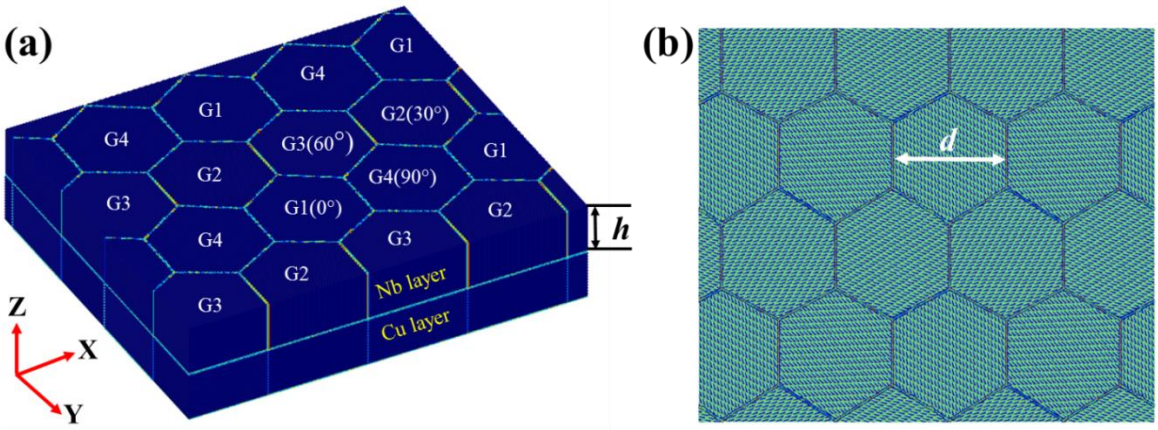

Figure 1. (a) Atomic scale configurations of nanograined Cu/Nb multilayers, (b) relaxed interface pattern in different grains (top view), colored according to the centro symmetry parameter [29]. (The directions for three axis are [1,$\bar{1}$,0]Cu||[$\bar{1}$,1,1]Nb in X axis, [1,1,$\bar{2}$]Cu||[1,$\bar{1}$,2]Nb in Y axis and [1,1,1]Cu||[1,1,0]Nb in Z axis.)

With all the above nanostructural aspects fixed, we then proceeded to create NL NC composites with different combinations of *d* and *h*. Many different grain sizes, *d*, were

used: 2.5, 5, 10 nm, 20 nm and 40 nm and as well as values of *h*, the layer thickness: 2.5 nm to 15 nm. The largest number of atoms in this model is about 15,000,000. In all cases of *h* and *d*, the grains had the same hexagonal shape and hence the same number of connecting triple junctions per grain.

Before loading, all NL composites were relaxed under the conditions associated with an isobaric isothermal ensemble (NPT [27], constant pressure and temperature) at zero pressure and 1 K for 300 ps via a Nose-Hoover temperature thermostat and pressure barostat [30,31]. This relaxation step allows the atoms to readjust their coordinates and settle into a lower energy state. Figure 1(b) shows the relaxed interface pattern for each pair of Cu/Nb grains according to the centro-symmetry parameter. These patterns are consistent with those reported in earlier work but for single crystalline (SX) Cu/Nb multilayers [32,33].

After relaxation, the NC NL composites are subjected to uniaxial tension parallel to the X-axis in Figure 1(a) such that Cu/Nb interfacial sliding would not be encouraged. In all cases to follow, we applied a constant strain rate of 5×10^{8} s^{-1}. The time interval for each simulation step was 1 fs.

3. RESULTS AND DISCUSSION

3.1. NANOSTRUCTURE EFFECTS ON STRESS-STRAIN RESPONSE

Upon loading the NC NL composites, leading Shockley partial dislocations initially emit from the grain boundary triple junctions, where the grain boundaries and interfaces meet, rather than from the bimetal interfaces. An example of this grain boundary dislocation emission (GBE) event is shown in Figure 2(a) and (b). The partials can be followed by a trailing partial either shortly afterwards, such that a full dislocation glides

across the grain as showed in Figure 2(c), or later in time after a stacking fault has already been formed across the grain by the leading Shockley partial. Secondly, we observe that the GBE occurs in both Cu and Nb as shown in Figure 2(d).

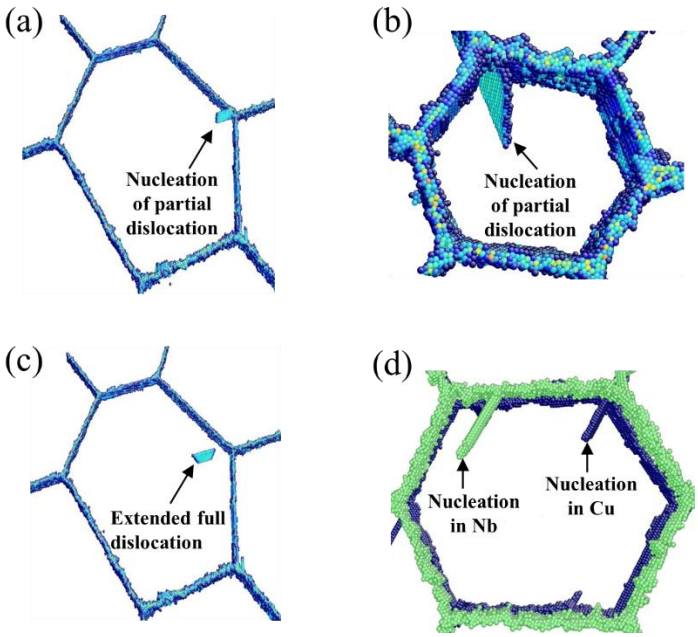

Figure 2. (a) The nucleation of partial dislocation from GB in Cu layer (d = 40 nm), (b) the nucleation of partial dislocation from GB in Cu layer (d = 10 nm), (c) extended full dislocation glide in Cu layer (d = 40 nm), and (d) the nucleation of partial dislocations from GB in both Cu and Nb layer (d = 20 nm), the interface atoms has been set as transparent.

These results have a few important distinctions from single crystalline (SX) NL composites. Such MD simulations have been reported earlier in this Cu/Nb KS system [7-10] but since some finer details in model set up and boundary conditions may be different, we carried out analogous simulations single crystalline (SX) NL composites and they are reported in the supplemental material section. Results presented there are consistent with those made previously. Firstly, under the same loading state, leading Shockley partial dislocations would initially emit from the bimetal interfaces in SX NL composites (see

Figure S2 in supplemental material). Secondly, dislocations emit into both phases in the NC NL composites, unlike in the SX NL where dislocations first emit into Cu and later into Nb. In NC NL composites, the preferred location for dislocation nucleation is the junction between interfaces and grain boundaries, since a large local stress concentration tend to develop at those sites.

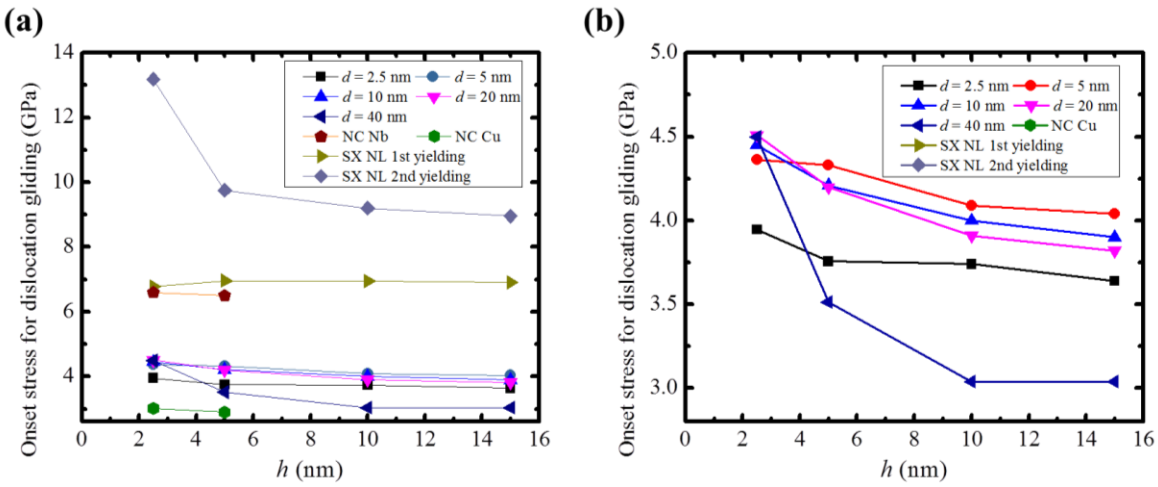

Figure 3. Plots of the onset stress for dislocation glide as a function of layer thickness, *h*, (a) for NC NL, SX NL, NC Nb and NC Cu, (b) only for NC NL.

Figure 3 show the onset stress for dislocation glide, while Figure 3(b) only consider the cases of NC NL composites and Figure 3(a) include the cases of SX NL and NC Cu. The stress-strain curve for all cases were shown in supplemental material. The effect of having nanocrystalline layers with grain boundaries is to weaken the NL relative to the ideal SX NL composite with the same *h*. This result implies that by virtue of how dislocations are nucleated that SX NL provides a practical upper bound to the strength of NC NL materials with the same *h*. This same viewpoint would, in turn, also suggest that nanocrystalline Cu (nc) with similar, equiaxed $h = d$ grain sizes would be even weaker, providing an apparent lower bound. These analogous simulations were also carried out

and checked against literature values (see supplement material Figure 1 and 2). Some strength values are reported in Figure 3(a). As expected, the strength of the NC NL composites lies between those of the SX NL and NC Cu for the same range of *h* and *d.* Relative to the NC Cu with the same grain width *d* and height *h*, the Cu/Nb interfaces in the NC NL substantially strengthen the material.

Thus we find that the introduction of grain boundaries cause the NC NL composites to become weaker relative to the SX NL for two reasons: the dislocations emit more easily from grain boundaries than the Cu/Nb interfaces and the GBE enables simultaneous plastic deformation in both Cu and Nb.

3.2. MECHANISMS GOVERNING YIELD STRESS

Figure 3(b) shows the variation in NC NL yield stress with *h* and *d.* Generally with respect to the yield stress, we observe the much anticipated scaling: smaller is stronger--as *d* and *h* both decrease, the yield stress increases. However, there are two exceptions. First, independent of *h*, a critical value d_s exists where d_s = 2.5 nm, the yield drops. Second, for the finest, *h* = 2.5 nm, the yield stress is highest at *d* = 20 nm and decreases with reductions in *d* from 10 nm to 2.5 nm. Interestingly, the NC Cu also exhibits the same trend; the yield stress is the highest for *d* = 20 nm and decreases with reductions in *d* from 10 nm to 2.5 nm. See Figure S1. In prior NC Cu simulations studies [34,35], this transition has been associated with a transition from slip-dominated deformation above the peak value *d* ~ 10 – 20 nm to grain boundary sliding-dominated deformation below. It would hint that even in NC NL composites, the grain boundaries or their spacing (grain sizes) in the nanocrystalline layers are driving the type of yield event. To determine more specifically the grain-boundary-driven mechanisms responsible for yield, we employ the atomic-shift

analysis to determine the strain at which dislocation emission and grain boundary sliding first occur in each nanolaminate. Figure 4 shows how the onset strain for GBE and GBS vary with *h* and *d.* For all *d* above d = 2.5 nm, the onset strain for dislocation emission is less than the onset strain for grain boundary sliding. Thus, emission of a dislocation from the grain boundaries marks the end of the linear regime and hence determines the true yield stress. The grain size d_s = 2.5 nm signifies a critical point when *d* is small enough that the onset strain for GBS (~0.045%) is lower than that for GBE and the onset of GBS is responsible for yield of the NC NL composite. For most values of *h,* d_s is also the value of *d* for which the yield strength of the material reduces rather than increases and the peak yield strength is realized for d = 5 nm, just above d_s. This behavior was not seen in the NC Cu cases, wherein the yield strength increased proportionally with increase in *d.*

The value of *d* at which *peak yield* is reached appears to be well correlated with the critical value of grain size d_s marking a transition from GBE to GBS. However, for the finest NC NL h = 2.5 nm, the peak yield is reached at d = 20 nm, well above d_s (see Figure 3(b)). For cases in which GBE governs composite yield ($d > d_s$), a further distinction between partial and full dislocation emission can be made. *Partial GBE* involves emission of a leading partial, which traverses the grain and forms a stacking fault across the grain, and emission of the trailing partial at a later time in strain. *Full GBE*, on the other hand, means that after the leading partial emits from the grain boundary, the trailing partial emits soon after, such that a full dislocation traverses the grain and no grain-scale stacking fault forms. As described earlier, the partial and full dislocations, particularly at the onset of yield, can be identified. Normally, larger grain can provide longer mean free path for the leading partial that leaves enough time for the trailing partials to emit from the GB and for

a full GBE. Employing the atomic-shift analysis technique at the onset strains for $d > d_s$, we find that for small d, $d < 10$ nm, partial GBE defines yield but for large $d > 20$ nm, full GBE marks the end of linear elastic deformation. The grain size $d = 20$ nm is a transition region when partial GBE occurs for larger h and full GBE for smaller h. Thus, in these NC NL composites, the yield strength can be sensitive to whether the first yield event is a partial or full GBE. Higher nucleation stresses are associated with full GBE.

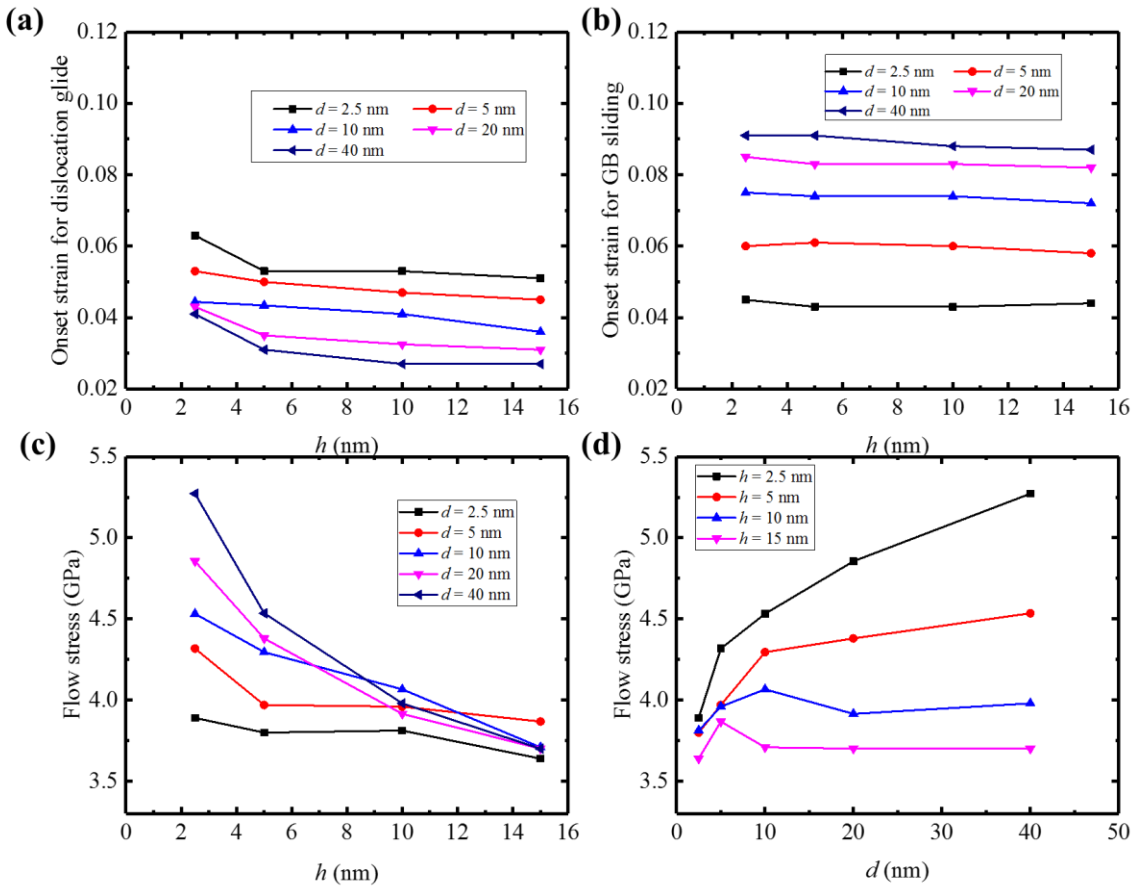

Figure 4. The strain for onset by (a) grain boundary dislocation emission and (b) GB sliding versus layer thickness. (c) The flow stress (average over 7% ~ 12% strain) vs layer thickness, h (d) the flow stress vs grain size d.

3.3. MECHANISMS GOVERNING FLOW STRESS

From Figure 4, we observe that in none of the NL nanostructures tested, does either GBS or GBE act alone throughout deformation. Rather it is observed that dislocation emission (whether partial or full) defines yield, with the exception of d_s = 2.5 nm, and GBS starts after dislocation emission. As d increases further beyond d_s, the more GBS is postponed and the more of the plastic strain is carried by dislocation glide. GBS, in these cases, are part of determining the flow stress after yield, but not yield. Likewise, for d = 2.5 nm, GBS may control the yield point, but GBE occurs shortly thereafter with more straining. We, therefore, can expect that the mechanisms governing the flow stress after yield would be different from those responsible for yield. Consequently the dependencies of flow stress on h and d would not necessarily follow those of the yield stress.

Specifically from the NC NL results in Figure 4, over the stress range of 7-12%, both GBE and GBS have initiated and the NC NL material is flowing with contributions from both mechanisms. Figure 4 (c) and (d) analyzes the variation of an average flow stress over the strain range of 7% – 12% with h, the conventional way to assess the strength of nanoscale NL. We considered minor adjustments to this strain range, only to find that they do not alter the trends reported here. It is observed in Figure 4 (c) and (d) that the NC NL flow stress increases as h decreases. Generally NL strengthening with smaller h in the nanoscale regime is often seen experimentally [17,28,36,37]. With respect to h, smaller leads to a higher flow stress. It is, however, a significant finding in Figure 4 (c) and (d) that the size scaling in h depends on d, weakening as d decreases. This result implies that to best exploit layer thickness h reductions for increasing strength (i.e., flow stress), the grain size d should be as large as possible.

Another important signature of the coupled effects of h and d is the crossing of the curves in Figure 4(c). To elucidate it, we plot in Figure 4(d), the same stress data for NC NL composites of fixed h with variation in d. For the larger h = 15 nm and 10 nm NC NL composites, a critical grain size d_c can be identified at which the composites achieves peak strength, which is 5 nm and 10 nm, respectively. For the finer h NC NL composites, h = 2.5 nm and 5 nm, the material weakens as d decreases. Evidently d_c is larger than 40 nm, the largest grain size tested here. The interesting finding is that in NC NL composites, a critical d_c exists and it depends on h, appearing to increase as h increases. This size scaling does not resemble the scaling in d for the NC Cu with no interfaces or the scaling in h for the SX NL composites with no grain boundaries.

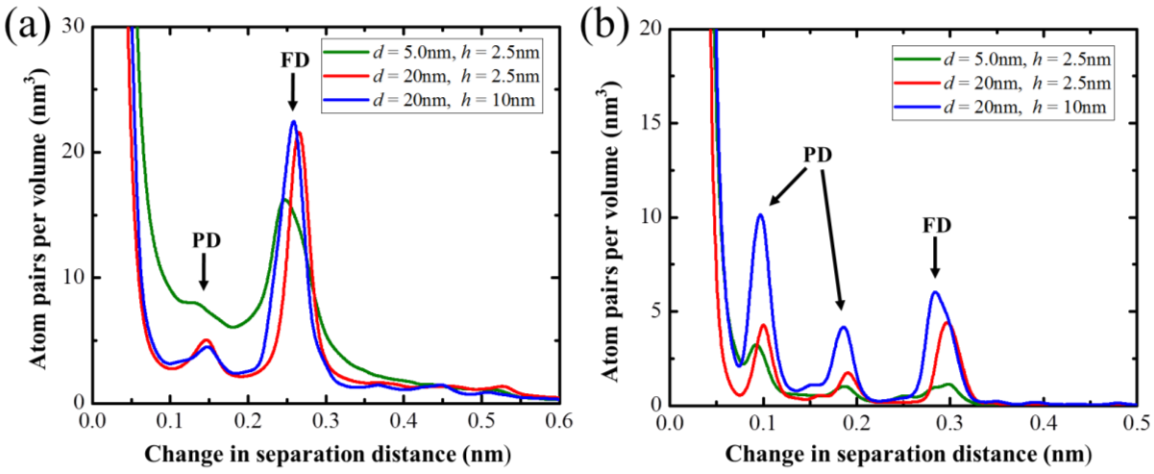

Figure 5. Histogram of the changes in the separation distance of initially nearest neighbor atoms after 10% strain in Cu layer (a) and Nb layer (b).

To understand how these size effects happen, we first calculate the atomic shifts in the material at 10% strain. The frequency plots for the atomic shifts for a few composites are shown in Figure 5. Two cases (h = 2.5 and d = 5 and 20 nm) lie in the softening regime e.g., $d < d_c$ (h), and the other one (h = 10 nm and d = 20 nm) in the hardening region, $d >$

d_c (h). Again, we see evidence of dislocation glide activity in both regimes. For the cases shown, we see that there is more dislocations gliding in Cu than Nb, both partial and full dislocations are gliding in Cu and Nb, and most of the dislocations are full dislocations in Cu while most of them are partial dislocations in Nb. Clearly, the amount of dislocation activity is linked strongly to the finest of the microstructural length scales, with less dislocation activity for finer h and d. However, dislocation glide contributes to carrying the strain whether the material strengthens or weakens with reduction in microstructure scales. Thus, there is not a clear abrupt transition in mechanisms that determines d_c.

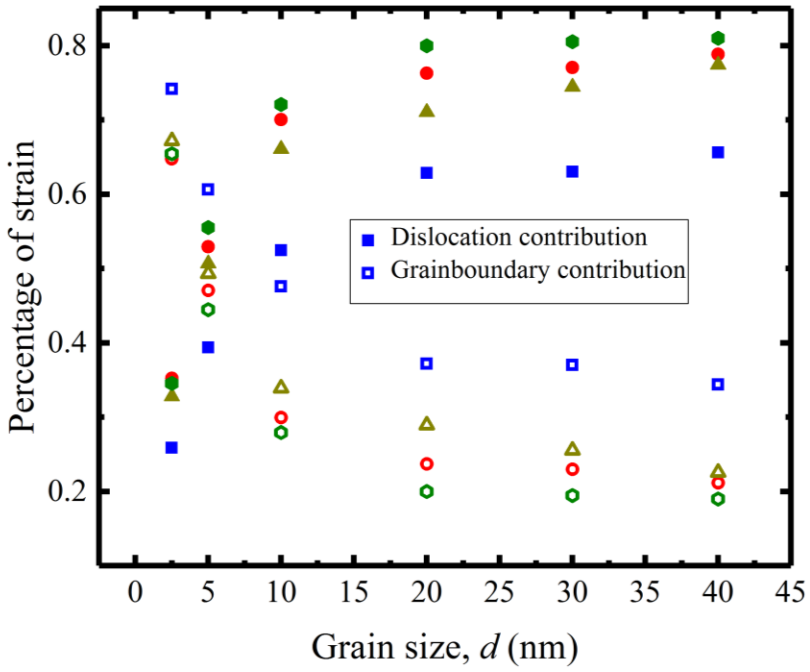

Figure 6. Comparison of the contributions in plastic strain from dislocation gliding (open symbols), and grain boundary sliding (solid symbols) at 10% total strain. (Squares for h = 2.5 nm, triangles for h = 5.0 nm, circles for h = 10nm and diamonds for h = 15 nm.)

From the atomic-shift analysis, the relative amounts of GBE and GBS can be assessed at any given strain. Figure 6 shows their relative contributions as a function of h

and *d*. We notice that in all cases, the strain throughout the deformation test is accommodated by a combination of GBE and GBS. The relative amounts of GBS increase as *d* deceases. For *d* = 5 nm, their contributions are nearly equivalent (~50%). For *d* = 2.5 nm, GB sliding dominates strain accommodation (> 60%). This analysis makes clear that for the range of *d* and *h* studied, GBE and GBS contribute to strain accommodation within the material. However, their relative amounts are sensitive to the two microstructural length scales *h* and *d*. The value of dc in flow stress corresponds to when the GBS contribution exceeds a threshold value of 25%, regardless of the value of *h*. Thus at the strongest nanoscale microstructural combination, dislocation glide will still carry most of the deformation (~75% or more). Further, at the transition size d_c, GBE defines yield and carries plasticity after yield.

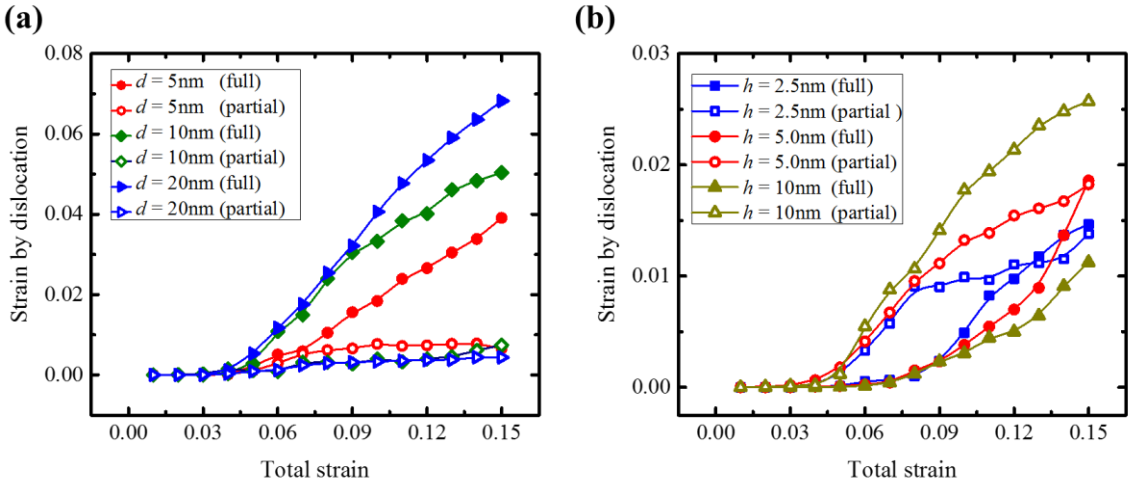

Figure 7. Strain contributions from dislocation slip for different samples in Cu layers: (a) h = 2.5 nm with different grain sizes, (b) *d* = 2.5 nm with different layer thicknesses.

From the foregoing analysis, we find that in most cases, dislocation glide mediates plastic strain. In such fine nanocrystals, partial slip rather than full slip is generally thought

to carry most of the strain. To determine the contribution of partial or full dislocation slip over the entire deformation response we applied atomic shift analysis. In Figure 7(a), we first show for h = 2.5 nm, a very finely layered nanolaminate for a range of grain sizes, 5 nm to 20 nm, wherein the GBE dominates the flow stress. In these cases, the first yield event is SF formation. However, from Figure 7(a), we see that after more strain, full dislocation glide dominates in all cases. In Figure 7(b), we analyze the evolution of dislocation activity in cases where GBS dominates ($d = d_s$). We see an interesting correlation between partial slip and GBS, partial glide dominates over the entire straining period. After emission, these dislocations glide across the crystal by threading through the layers. Theoretically, the finer h, the more stress required for an individual dislocation to push through ~log(h)/h. Consequently, the finer h, the higher the flow stress. Unlike, the yield stress associated with stress to emit the first dislocations, depends on h. This effect can be seen in Figure 7(b), as h decreases, more total applied strain is needed to achieve the same dislocation strain.

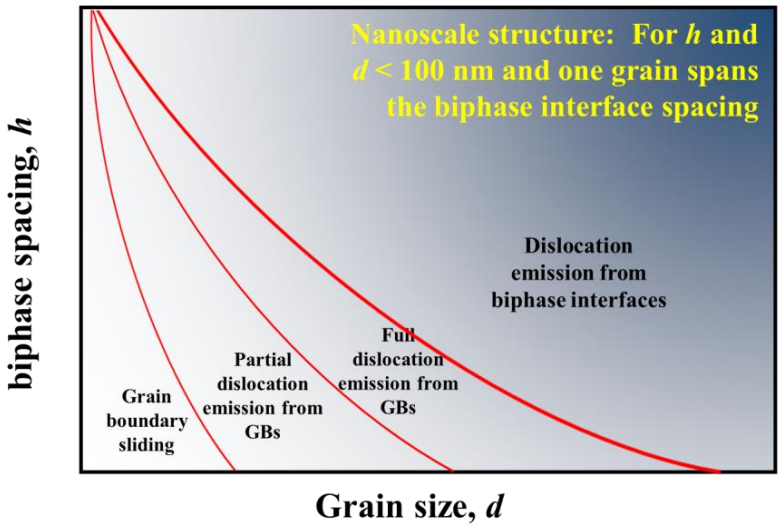

Figure 8. Generalized mechanism map for the first yield event in strained NC NL composites.

The present simulation results on Cu/Nb nanolayers and those from a recent similar study on polycrystalline Cu/Ag nanolayers[14] help to clarify the size-driven mechanisms that affect the yield stress of NC NL To illustrate this, Figure 8 maps the regimes for the predominant deformation mechanisms underlying yield on a plot with axes *h* and *d.* This map would apply to nanoscale materials in which only one grain spans the layer thickness *h* and the grains are *d* in width and both *d* and *h* have nanoscale dimensions (< 100 nm, such as in Figure 1). At one end of the map, with large *d*, yield is determined by first emission of a dislocation from the biphase interface. At the other end, with small *d*, yield is determined by grain boundary sliding. In between, as *d* and *h* increase yield is governed by emission of partials and full dislocations from the grain boundaries.

4. CONCLUSIONS

In summary, we use atomic-scale simulation to investigate microstructural size scaling in the strength of nanocrystalline nanolayered (NC NL) Cu/Nb composites. Scalings in both the intralayer NC grain size *d* and layer thickness *h* were investigated. The calculations reveal strongly coupled *d-h* effects. Unlike single crystalline nanolayered composites without grain boundaries, where plasticity is initiated by emission of dislocations from the interfaces into preferably one of the phases, in the NC NL composites, dislocations are emitted from the junctions were grain boundaries and interfaces meet and within both phases. Both phases, thus, participate in yield and plastic flow in NC NL. Further, the grain size *d* controls the yield phenomenon, with the finest of grain sizes $d \leq d_s$, yielding via intralayer grain boundary sliding (GBS), and the larger grain sizes $d > d_s$, yielding by intralayer grain boundary dislocation emission (GBE). Grain size *d* also

governs the relative amounts contributed by GBE and GBS during plastic flow stress after the defining first yield event has occurred. The highest flow stress (strongest) NC NL occurs at a grain size d_c, the grain size below which the percentage contribution of GBS equals or increases greater than 25%. As GBS becomes increasingly hindered as *h* increases, the value of the "strongest size d_c" for the NC NL composite decreases as *h* increases. Last, the intragranular grain boundary spacing *d* also affects the sensitivity of NC NL strength to reductions in *h*. Partial dislocation activity occurs when GBS dominates and the effect of *h* on strength is weak, whereas full dislocation activity prevails when GBS is small (< 60%) and the smaller the amounts of GBS, the greater gains in strength with reduction in *h*. The grains should be as large as possible to best reap the strengthening benefits of reductions in layer thickness.

The foregoing results on layer *h* size and intralayer *d* effects in NC NL composites make clear that the average size *d* of the grains in the nanocrystalline layers is a highly influential variable for strength. In most cases, the grain sizes among NL composites of different *h* are not reported or not the same. These findings can help to better interpret *h*-scale effects on measure yield or flow strength.

5. METHODS

To identify the mechanisms responsible for deformation, we used two procedures. AtomEye [38] was used to visualize the configuration of atoms in the microstructure. The second one is denoted here as the atomic-shift analysis and is built upon the methods provided by Vo et al. [39] for nanocrystalline fcc metals. This analysis determines the relative amounts of partial dislocation glide, full dislocation glide, and grain-boundary-mediated

deformation. In brief, the first step involves identifying the atoms in the grain interiors using the Common neighbor analysis (CNA) [25,40]. The second step calculates the pair separation (PS) for the atoms in grain interiors. PS is a measure of the relative motion between nearest neighbor pairs of atoms compared to its initial value. From this analysis, we can evaluate the frequency of atomic shifts for the entire system at any given strain level during deformation. Characteristic amounts of shifts in these plots correspond to the Burgers vector of either partial or full dislocations. More details of this method are given in Vo et al. [39]. Further, from these atomic shifts, the amount of strain contributed by partial or full dislocation glide can be calculated by summing the strain induced by all atoms displaced by dislocation motion, as follows:

$$\varepsilon^{dis} = \sum_i^N \frac{A}{V} \times (\bar{l} \cdot \bar{b}_i) \times (\bar{l} \cdot \bar{n}_i) \quad (1)$$

where $\bar{b}_i$ is the Burgers vector of the dislocation slipping over the atom i, $\bar{n}_i$ is the unit normal of the slip plane for the dislocation slipping over the atom i, $\bar{l}$ is the loading direction, A is the unit area of atoms projected on the slip plane, V is the volume of the simulation box, and N is the total number of slipped atom.

All other atomic shifts not associated with dislocation glide are attributed to grain boundary deformation, such as grain boundary sliding (GBS) and diffusion. Since the current simulations are carried out a 1K, it is likely that these atomic shifts can be attributed predominantly to grain boundary sliding (GBS). In this article, the atomic-shift analysis is used to determine the onset strain and the relative contributions of dislocation glide or GBS to accommodating strain at any strain level.

ACKNOWLEDGEMENTS

This work was supported by the grants from NSF CAREER Award (CMMI-1652662). S.H. is also grateful for the partial support provided by The University of Missouri Research Board. IJB acknowledges financial support from the National Science Foundation (NSF CMMI-1729887).

REFERENCES

1 Höchbauer, T., Misra, A., Hattar, K. & Hoagland, R. Influence of interfaces on the storage of ion-implanted He in multilayered metallic composites. Journal of applied physics 98, 123516 (2005).

2 Misra, A., Hirth, J., Hoagland, R., Embury, J. & Kung, H. Dislocation mechanisms and symmetric slip in rolled nano-scale metallic multilayers. Acta materialia 52, 2387-2394 (2004).

3 Wang, Y.-C., Misra, A. & Hoagland, R. Fatigue properties of nanoscale Cu/Nb multilayers. Scripta materialia 54, 1593-1598 (2006).

4 Misra, A., Demkowicz, M., Zhang, X. & Hoagland, R. The radiation damage tolerance of ultra-high strength nanolayered composites. Jom 59, 62-65 (2007).

5 Beyerlein, I. J. et al. Emergence of stable interfaces under extreme plastic deformation. Proceedings of the national academy of sciences, 201319436 (2014).

6 Misra, A. & Hoagland, R. Effects of elevated temperature annealing on the structure and hardness of copper/niobium nanolayered films. Journal of materials research 20, 2046-2054 (2005).

7 Wang, J., Zhou, C., Beyerlein, I. J. & Shao, S. Modeling interface-dominated mechanical behavior of nanolayered crystalline composites. Jom 66, 102-113 (2014).

8 Mastorakos, I. N., Bellou, A., Bahr, D. F. & Zbib, H. M. Size-dependent strength in nanolaminate metallic systems. Journal of Materials Research 26, 1179-1187 (2011).

9 Wang, J., Hoagland, R., Hirth, J. & Misra, A. Atomistic modeling of the interaction of glide dislocations with “weak” interfaces. Acta materialia 56, 5685-5693 (2008).

10 Abdolrahim, N., Zbib, H. M. & Bahr, D. F. Multiscale modeling and simulation of deformation in nanoscale metallic multilayer systems. International Journal of Plasticity 52, 33-50, doi:10.1016/j.ijplas.2013.04.002 (2014).

11 Martínez, E., Caro, A. & Beyerlein, I. J. Atomistic modeling of defect-induced plasticity in CuNb nanocomposites. Physical review b 90, 054103 (2014).

12 Zhou, J., Averback, R. & Bellon, P. Stability and amorphization of Cu–Nb interfaces during severe plastic deformation: Molecular dynamics simulations of simple shear. Acta Materialia 73, 116-127 (2014).

13 Beyerlein, I., Demkowicz, M., Misra, A. & Uberuaga, B. Defect-interface interactions. Progress in Materials Science 74, 125-210, doi:10.1016/j.pmatsci.2015.02.001 (2015).

14 Zhu, Y., Li, Z. & Huang, M. The size effect and plastic deformation mechanism transition in the nanolayered polycrystalline metallic multilayers. Journal of Applied Physics 115, 233508 (2014).

15 Zhu, Y., Li, Z., Huang, M. & Liu, Y. Strengthening mechanisms of the nanolayered polycrystalline metallic multilayers assisted by twins. International Journal of Plasticity 72, 168-184 (2015).

16 Li, N., Wang, J., Huang, J., Misra, A. & Zhang, X. In situ TEM observations of room temperature dislocation climb at interfaces in nanolayered Al/Nb composites. Scripta Materialia 63, 363-366 (2010).

17 Misra, A., Hirth, J. & Hoagland, R. Length-scale-dependent deformation mechanisms in incoherent metallic multilayered composites. Acta materialia 53, 4817-4824 (2005).

18 Mara, N. A. & Beyerlein, I. J. Review: effect of bimetal interface structure on the mechanical behavior of Cu–Nb fcc–bcc nanolayered composites. Journal of materials science 49, 6497-6516, doi:10.1007/s10853-014-8342-9 (2014).

19 Meyers, M. A., Mishra, A. & Benson, D. J. Mechanical properties of nanocrystalline materials. Progress in materials science 51, 427-556 (2006).

20 Liu, X., Zhang, H. & Lu, K. Strain-induced ultrahard and ultrastable nanolaminated structure in nickel. Science 342, 337-340 (2013).

21 Gianola, D. et al. Stress-assisted discontinuous grain growth and its effect on the deformation behavior of nanocrystalline aluminum thin films. Acta Materialia 54, 2253-2263 (2006).

22 Rupert, T., Gianola, D., Gan, Y. & Hemker, K. Experimental observations of stress-driven grain boundary migration. Science 326, 1686-1690 (2009).

23 Plimpton, S. Fast Parallel Algorithms for Short-Range Molecular Dynamics. Journal of Computational Physics 117, 1-19, doi:https://doi.org/10.1006/jcph.1995.1039 (1995).

24 Zhang, L., Martinez, E., Caro, A., Liu, X.-Y. & Demkowicz, M. J. Liquid-phase thermodynamics and structures in the Cu–Nb binary system. Modelling and Simulation in Materials Science and Engineering 21, 025005, doi:10.1088/09650393/21/2/025005 (2013).

25 Honeycutt, J. D. & Andersen, H. C. Molecular dynamics study of melting and freezing of small Lennard-Jones clusters. Journal of Physical Chemistry 91, 4950-4963 (1987).

26 Daw, M. S. & Baskes, M. I. Embedded-atom method: Derivation and application to impurities, surfaces, and other defects in metals. Physical Review B 29, 6443, doi:10.1103/PhysRevB.29.6443 (1984).

27 Schiøtz, J., Vegge, T., Di Tolla, F. & Jacobsen, K. W. Atomic-scale simulations of the mechanical deformation of nanocrystalline metals. Physical Review B 60, 11971, doi:10.1103/PhysRevB.60.11971 (1999).

28 Hoagland, R. G., Kurtz, R. J. & Henager, C. H. Slip resistance of interfaces and the strength of metallic multilayer composites. Scripta materialia 50, 775-779, doi:10.1016/j.scriptamat.2003.11.059 (2004).

29 Kelchner, C. L., Plimpton, S. & Hamilton, J. Dislocation nucleation and defect structure during surface indentation. Physical review B 58, 11085 (1998).

30 Hoover, W. G. Constant-pressure equations of motion. Physical Review A 34, 2499-2500, doi:10.1103/PhysRevA.34.2499 (1986).

31 Nosé, S. A unified formulation of the constant temperature molecular dynamics methods. The Journal of chemical physics 81, 511-519, doi:/10.1063/1.447334 (1984).

32 Wang, J., Zhang, R., Zhou, C., Beyerlein, I. J. & Misra, A. Characterizing interface dislocations by atomically informed Frank-Bilby theory. Journal of Materials Research 28, 1646-1657 (2013).

33 Wang, J., Zhang, R. F., Zhou, C. Z., Beyerlein, I. J. & Misra, A. Interface dislocation patterns and dislocation nucleation in face-centered-cubic and body-centered-cubic bicrystal interfaces. International Journal of Plasticity 53, 40-55 (2014).

34 Schiøtz, J., Di Tolla, F. D. & Jacobsen, K. W. Softening of nanocrystalline metals at very small grain sizes. Nature 391, 561-563, doi:10.1038/35328 (1998).

35 Van Swygenhoven, H., Caro, A. & Farkas, D. A molecular dynamics study of polycrystalline fcc metals at the nanoscale: grain boundary structure and its influence on plastic deformation. Materials Science and Engineering: A 309, 440-444, doi:10.1016/S0921-5093(00)01794-9 (2001).

36 Tokarz, A., Fraczek, T., Balaga, Z. & Nitkiewicz, Z. Structure, hardness and thermal stability of electrodeposited Cu/Ni nanostructured multilayers. Rev. Adv. Mater. Sci 15, 247 (2007).

37 Misra, A., Kung, H., Hammon, D., Hoagland, R. & Nastasi, M. Damage mechanisms in nanolayered metallic composites. International Journal of Damage Mechanics 12, 365-376, doi:10.1177/105678903036227 (2003).

38 Li, J. AtomEye: an efficient atomistic configuration viewer. Modelling and Simulation in Materials Science and Engineering 11, 173, doi:10.1088/0965-0393/11/2/305 (2003).

39 Vo, N., Averback, R., Bellon, P., Odunuga, S. & Caro, A. Quantitative description of plastic deformation in nanocrystalline Cu: Dislocation glide versus grain boundary sliding. Physical Review B 77, 134108, doi:10.1103/Physrevb.77.134108 (2008).

40 Faken, D. & Jónsson, H. Systematic analysis of local atomic structure combined with 3D computer graphics. Computational Materials Science 2, 279-286, doi:10.1016/0927-0256(94)90109-0 (1994).

II. FRACTURE RESISTANCE OF CU/NB METALLIC NANOLAYERED COMPOSITE

Sixie Huang[1] and Caizhi Zhou[1]

Department of Materials Science and Engineering, Missouri University of Science and Technology, Rolla, MO 65409, USA

Submitted in Journal of Materials Research

ABSTRACT

In this work, we perform molecular dynamics simulations to explore the crack propagation and fracture behavior of Cu/Nb metallic nanolayered composites (MNCs). Our results are consistent with previous experimental results, which illustrated that cracks in Cu and Nb layers may exhibit different propagation paths and distances under the same external loading. The analysis reveals that the interface can increase the fracture resistance of the Nb layer in Cu/Nb MNCs by providing the dislocation sources to generate the plastic strain at the front of the crack. Increasing the layer thickness can enhance the fracture resistance of both Cu and Nb layers, as the critical stress for activating the dislocation motion decreases with the increment of the layer thickness. In addition, grain boundaries (GBs) in polycrystalline Cu/Nb samples would decrease the fracture resistance of Nb layer by promoting the crack propagate along the GBs, i.e. intergranular fracture, while the effect of interface and layer thickness on the fracture resistance of MNCs will not be altered by introducing the GBs in MNCs.

Keywords: Nanolayer; Interface; Fracture behavior; Atomistic modeling; Crack propagation

1. INTRODUCTION

Metallic nanolayered composites (MNCs) are nanostructured materials possessing impressive mechanical properties such as high strength, hardness and fatigue resistance, which can be fabricated by deposition or severe plastic deformation processes [1-6]. MNCs are composed of alternating layers of two or more metallic phases and the layer thickness of each phase are generally less than 100 nm. The interfaces between each layer play an critical role on the deformation of MNCs, as they can act as barriers, sink and sources of dislocations and vacancies [7-9]. Both experimental and computational studies have illustrated the remarkable thickness-dependent strength in MNCs that can be predicted by the confined layer slip (CLS) model [10-13]. Similar to nanocrystalline (NC) metallic materials, MNCs also exhibits an inverse relationship between the strength and elongation [12,14]. To explore the fracture mechanisms in MNCs, Zhu at el. [15] examined the deformation zone ahead of the crack tip in the Cu/Ta MNCs and revealed a critical layer thickness, below which the fracture mode of the MNCs tends to be shearing failure. Zhang at el. [16] studied the fracture behavior of Cu/Nb and Cu/Zr. Their experiment results demonstrated that as the layer thickness of Cu layer decreased below 60 nm, the fracture mode in MNCs transited from brittle opening fracture to shear fracture. Based on their experiment results, they claimed that the transition of fracture modes is dominated by the constraint of the soft Cu layer on the brittle Nb or Zr layer. Liang et al. [17] performed the tensile tests on Cu/Ni MNCs and revealed a transition of fracture modes from necking-inhibited brittle mode to necking-delayed ductile mode as the Ni layer thickness decrease from 90 to 40 nm. Hattar et al. [18] demonstrated four fracture steps (crack deviation, layer necking, microvoid

formation and crack blunting) during the crack propagation in Cu/Nb by using the in-situ transmission electron microscopy testing.

Based on previous studies, we can see that in most MNCs, the plastic deformation ability is limited by the thickness of each single layered phase. The interface in the MNCs can not only influence the strength of MNCs but also affect their ductility and the fracture behaviors. However, it is still unclear how the interface in MNCs affects the fracture mode of MNCs and how the crack interacts with the interface under external loading. Atomistic simulations, such as molecular dynamics (MD) simulations, can shed light onto the failure mechanisms of NC materials by directly revealing the underlying atomic scale processes of the deformation and fracture. Fracture behavior for NC metals, nanotwinned metals and gradient metals have had been explored by previous atomistic simulations [19-21]. In this study, we perform MD simulations of the deformation in Cu/Nb MNCs with a preexisting crack to explore the crack propagation and fracture behavior of MNCs. Our simulation results show that the interface can increase the fracture resistance of the brittle Nb layer by providing the dislocation sources to generate the plastic strain at the front of the crack. The fracture resistance of both layers would be enhanced by increasing the layer thickness. Introducing grain boundaries (GBs) would decrease the fracture resistance of Nb layer, as he GBs act as the weakest location promoting the intergranular fracture.

2. MATERIALS AND METHODS

We perform the MD simulation by using Large-scale Atomic/Molecular Massively Parallel simulator (LAMMPS) codes [22]. Interatomic potentials based on the Embedded Atom Method (EAM) was used to describe the force between each atom. Potential

developed by Mishin et al. , Ackland et al. and Zhang et al. were used to describe the interatomic force for Cu-Cu, Nb-Nb and Cu-Nb respectively [2,23,24]. These potential have been used widely in the last decade for many studies and provided insight for understanding the deformation mechanism [25-28].

To study the effect of interface and the coupled effect of interface and grain boundaries on fracture behavior of MNCs, we adopt multiple types of samples in our model which include two-phase samples of single crystalline (SX) Cu/Nb, polycrystalline (PX) Cu/Nb, and single phase samples of SX Cu, SX Nb, PX Cu, PX Nb. Figure 1 presents the examples of samples used in our calculations. Periodic boundary conditions have been applied along the thickness direction, while a fixed boundary condition was set in the other two directions under external loading. A pre-existing crack is created with the crack tip end at the center of each sample. To mimic the microstructure of Cu/Nb composites synthesized by the physical vapor deposition method (PVD) [29], the crystallographic orientation for the Cu layer is set as x-[11-2], y-[1-10], and z-[111], while the crystallographic orientation for the Nb layer is set as x-[11-2], y-[111], and z-[1-10]. This configuration of Cu and Nb phases follows the Kurdjumov-Sachs (KS) orientation relationship [30]. In the PX Cu/Nb samples, a modified Voronoi method [31] was used to create the nano grains with a hexagonal grain shape shown in Figure 1(b). The grain size for PX samples in this study was set to be 10nm. We fixed one pair of Cu/Nb grains with the initial crystallographic orientation described above and rotated the neighboring grain pairs by 30°, 60° and 90° degree along the thickness direction shown in Figure 1 (b). In this way, stable large angle GBs can be created and the KS orientation relationship can still be maintained in each of pair the Cu/Nb grains. Finally, to explore how the layer thickness affects the fracture behavior of MNCs,

we vary the layer thickness of both SX Cu/Nb and PX Cu/Nb samples from 5 nm to 20 nm in our model.

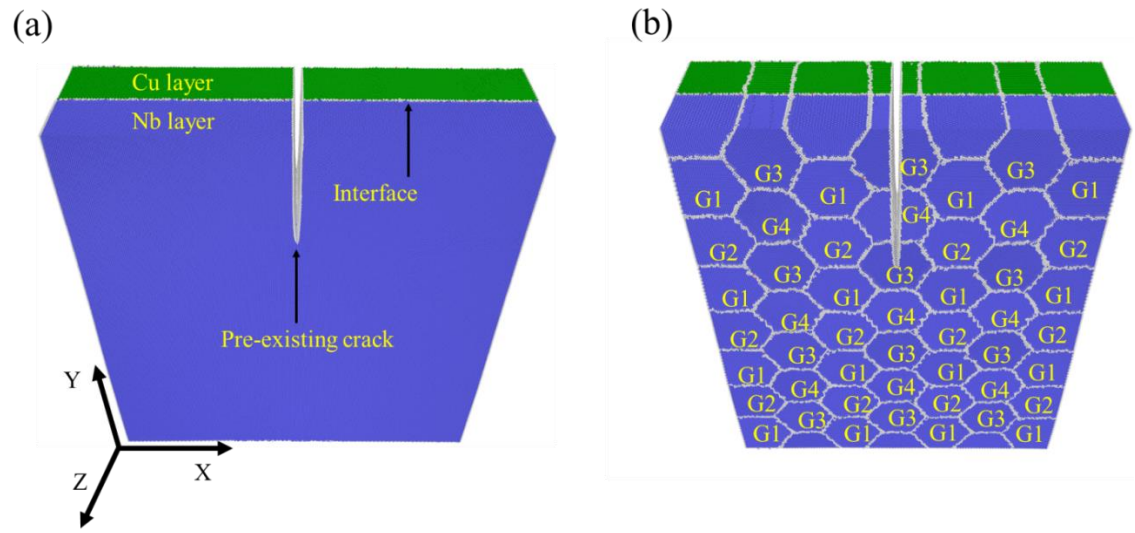

Figure 1. Initial configuration of Cu/Nb samples with a preexisting crack: (a) single crystalline (SX) Cu/Nb sample, (b) polycrystalline (PX) Cu/Nb samples. (Atoms colored by the CAN method. Atoms with green, blue and white represent the FCC, BCC and unknown atoms, respectively. The unknown atoms general represents the atoms locate at grain boundaries and interface.) The crystallographic orientation for Cu layer is set as x-[11$\bar{2}$], y-[1$\bar{1}$0], and z-[111], while the crystallographic orientation for Nb layer is set as x-[11$\bar{2}$], y-[111], and z-[1$\bar{1}$0]. G1 have the same crystallographic orientation in (a), G2, G3, G4 were rotated by 30°, 60° and 90° degree along the Z-axis.

Before experiencing loading, the samples were relaxed by the conjugate gradient method, then equilibrated at 300K for about 40 ps by the Nose/Hoover isobaric-isothermal ensemble (NPT) [31] and the pressure in the Z direction was kept at zero [32,33]. After relaxation, we load the sample by increasing the stress intensity factor of $0.015\ \mathrm{MPa}\sqrt{m}$ per step based on the fracture mechanics solution for mode-I fracture [19]. During each loading step, the boundary atoms within 1 nm from the edge in X and Y directions were fixed while other mobile atoms were allowed to relax for 1 ps. The crack tip was recorded to extract

the crack length at a specific applied strain. Common neighbor analysis method [24] and Green strain tensor [34] were calculated to characterize the microstructure evolution. Dislocation structures were generated by the dislocation extraction algorithm (DXA) [35]. Finally, the atomistic structures were visualized by the software OVITO [36].

To determine Greens strain, $\boldsymbol{E}_{ij}$, for each atom, we calculated the local deformation gradient tensor $\boldsymbol{F}$ for each atom based on the derivative of the relative displacements of the atom's neighbors

$$\boldsymbol{F}_{iI} = \frac{\partial x}{\partial X} \tag{1}$$

where $\mathbf{X} = [X_1, X_2, X_3]$ is the original distance vector for atoms to their references before deformation, and $\mathbf{x} = [x_1, x_2, x_3]$ is the new distance vector during deformation. The neighboring atoms should locate within a cutoff radius for 3.5 Angstrom, which can include at least three non-coplanar neighbors for the targeted atom [37]. Then Greens strain E_{ij} is calculated by:

$$\boldsymbol{E}_{ij} = \frac{1}{2}(\boldsymbol{F}_{iI}\boldsymbol{F}_{ij} - \delta_{IJ}) \tag{2}$$

where δ_{IJ} is the identity tensor.

3. RESULTS AND DISCUSSION

3.1. SINGLE CRYSTALLINE SAMPLES WITHOUT GRAIN BOUNDARIES

Figure 2 shows the atomistic structure for different SX samples at 15% engineering strain. The atoms in these figure were colored by the Green strain component ε_{xx}.. Figure 2 (a)-(c) present the samples for SX Cu, Cu layers in 5nm and 20 nm SX Cu/Nb samples, respectively. Crack tips in Cu for all three samples were blunted. The crack in SX Cu and Cu layer in 20nm SX Cu/Nb samples traveled almost the same distance at 15% strain, while

the crack length in Cu layer of 5nm SX Cu/Nb sample is pronounced longer than the previous two cases. Figure 2 (d)-(f) present the shape and propagation path of the crack in SX Nb, Nb layer of 5 nm and 20 nm SX Cu/Nb samples. It is obvious that the final lengths of the crack in Nb layer of SX Cu/Nb samples are shorter than that in the SX Nb sample. In addition, the larger the layer thickness of the SX Cu/Nb samples, the shorter the crack length is.

The specific crack tip propagation distances versus the applied strain for all samples are shown in Figure 3 (a). We can see that the crack propagation distances in SX Cu or Cu layers of SX Cu/Nb samples are all below 75 Å. The crack propagation distances are always larger in SX Nb or Nb layer of SX Cu/Nb samples than that in Cu. Therefore, even if the initial preexisting crack position are the same in both Cu and Nb layers in Cu/Nb samples, crack propagation path and distance may be different for each phase in MNCs. This trend is consistent with experiment results [18] that the crack grows faster in the Nb layer than in the Cu layer as shown in Figure 4.

Among the SX Nb sample and the Nb layer of SX Cu/Nb samples, the SX Nb sample has the largest crack propagation distance and fastest propagation rate shown in Figure 3 (a). It indicates that Cu/Nb interface can slow down the crack propagation rate and increase the fracture resistance ability in the Nb layer. At 15% strain, the crack propagated distance has been decreased by 42% from 21 nm in SX Nb to 12 nm in the Nb layer of 5nm SX Cu/Nb. Moreover, the improvement of fracture resistance is more prominent in the thicker Nb layer. Compared to the SX Nb sample, the final propagation distance for the Nb layer in the 20nm SX Cu/Nb decrease from 21 to 6 nm. Thus, the thicker the sample, the better the crack resistance is in the Nb layer. This trend is also consistent

with the results from a previous experimental study by Kavarana et al. [14], which demonstrated that that the ductility of MNCs increases with the bilayer thickness.

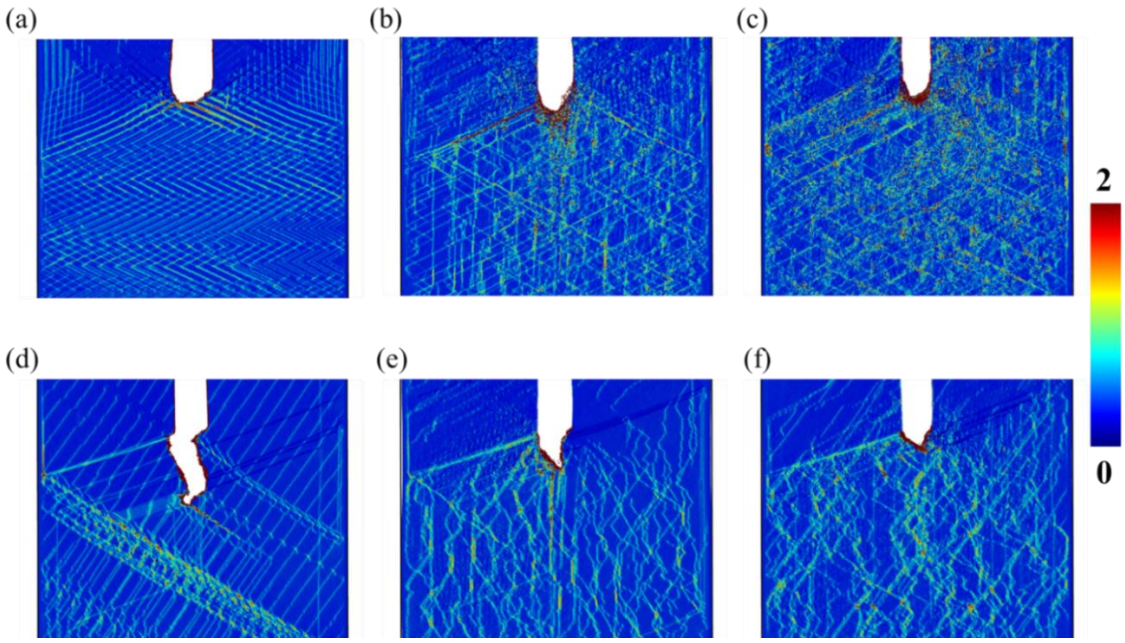

Figure 2. Atomistic structures for samples at 15% strain, atoms colored by the green strain component, ε_{xx}. (a) SX Cu, (b) Cu layer in 5 nm SX Cu/Nb, (c) Cu layer in 20 nm SX Cu/Nb, (d) SX Nb, (e) Nb layer in 5 nm SX Cu/Nb, (f) Nb layer in 20 nm SX Cu/Nb.

Figure 3 (b) shows the evolution of the stress intensity factor (SIF) versus the crack tip propagation distance. Similar to the trend shown in Figure 3 (a), SX Cu and Cu layer in Cu/Nb samples have larger SIF than those in the SX Nb and Nb layer in Cu/Nb. And SX Cu and Cu layer in 20 nm SX Cu/Nb carry similar values of SIFs over the same crack tip propagation range and both are larger than that for the Cu layers in 5nm the SX Cu/Nb sample. In addition, the SIFs for the Nb layer in Cu/Nb samples are larger than that for the SX Nb. Additionally, the larger the layer thickness, the higher SIFs of each phase in Cu/Nb samples.

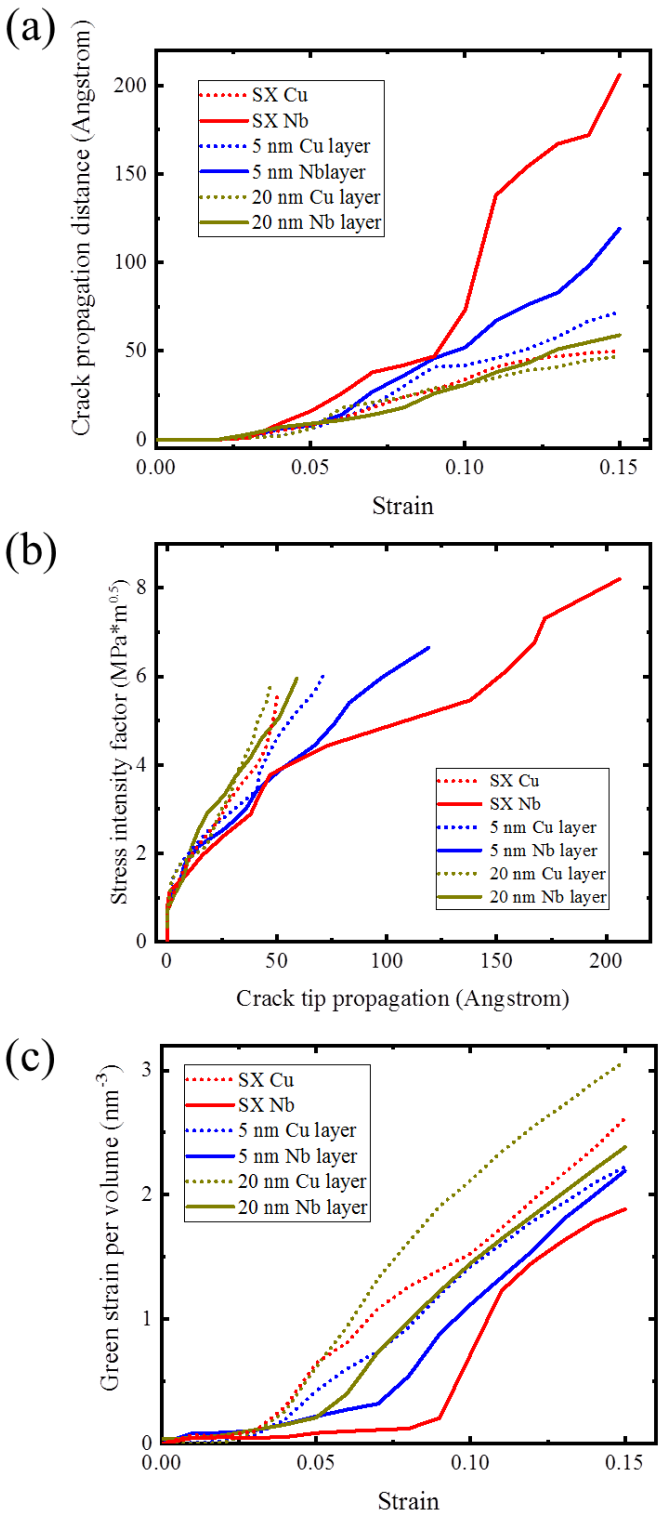

Figure 3. (a) Plot of crack propagation distance for different SX samples. (b) Stress intensity factor curves for different SX sample. (c) Green strain per volume for different SX samples.

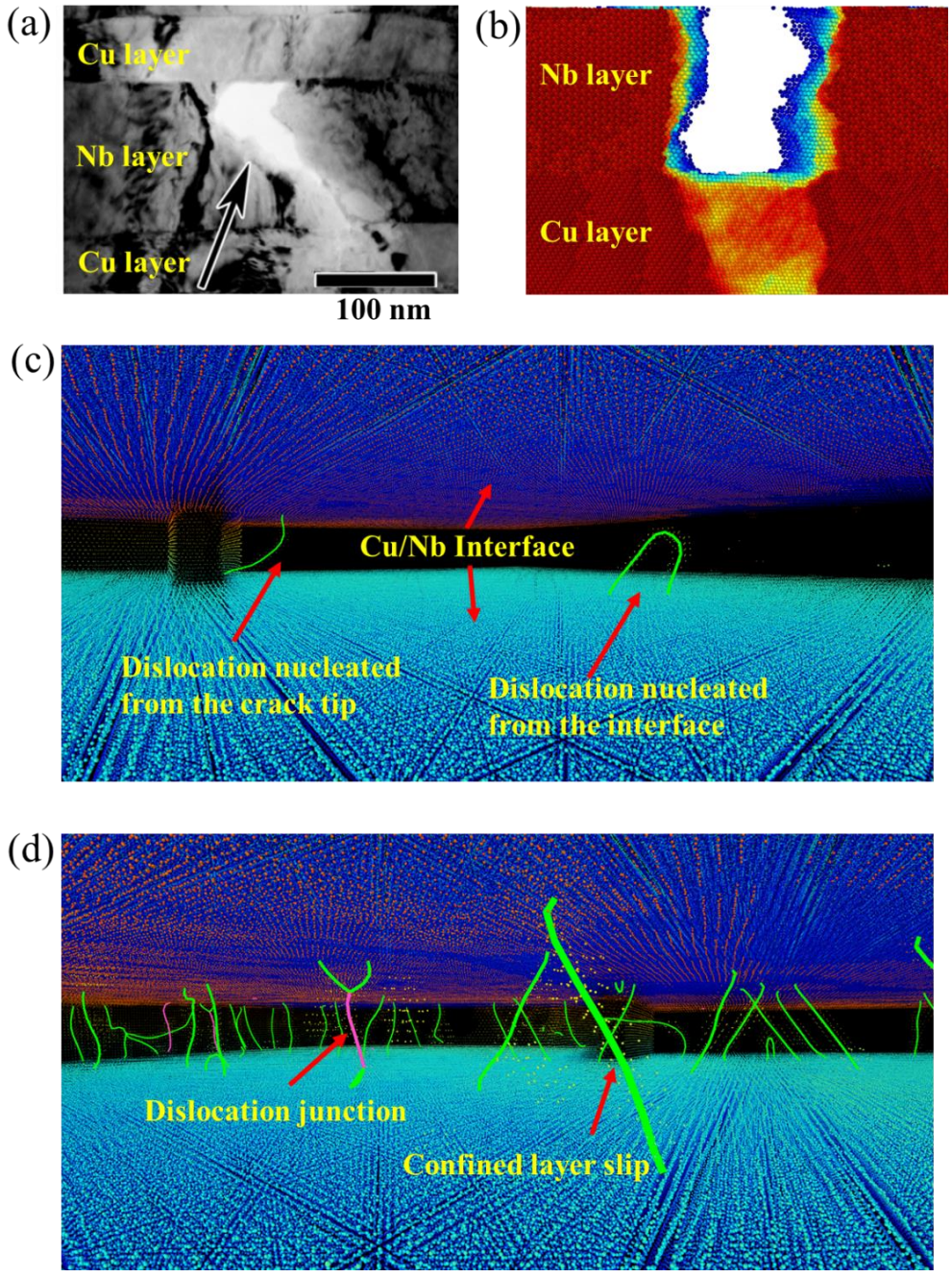

Figure 4. (a) One crack in Cu/Nb MNCs from the experimental work [18]. (b) One crack in SX Cu/Nb samples in this study (The fractured layer is Nb layer and atoms were colored by their Y coordinate. Note: the crack growth direction is perpendicular to the paper in both experimental and simulation tests). (c) Dislocation nucleating from the interface and crack tip (Atoms with BCC type were set invisible. Atoms were colored by their Z coordinate. Dislocations with green colors is for 1/2 <111> in {110} slip system.). (d) Confined layer slip of dislocations. (Dislocations with purple colors represent the dislocation junction.)

Since no GBs exist in all SX samples, Greens strain shown in Figure 2 should totally result from the dislocation activities. The Greens strains in Nb layers of SX Cu/Nb samples are more uniform than that in the SX Nb sample. That indicates each slip system in the Nb layer of SX Cu/Nb samples carry a similar amount of plastic deformation induce by dislocation activities, while the dislocation activities were more focused on one or two slip systems in SX Nb sample. Figure 3 (c) compares the total Greens strains induced by dislocation activities per volume for SX samples. It is clear that at the same applied strain, the Green strains induced by dislocation activities are higher in SX Cu and Cu layer in Cu/Nb than those in the Nb phase or layers. The evolution of the Green strain in each case is consistent with the crack propagation distance shown in Figure 3(a) and SIFs in Figure 3(b). The phase with higher SIF and shorter crack propagation distance normally contains larger Green strain. In metallic materials, there are two ways to release the excess elastic energy stored within the materials: i) creating new surfaces by opening cracks, or ii) changing the shape of the material via plastic deformation. In the SX samples, the plastic deformation was mainly induced by the dislocation activities. Thus, larger Green strain under the same applied strain indicates more plastic deformation induced by dislocation activaties that suppressed the crack propagation to create new surfaces. In the Cu/Nb samples, the interface provides dislocation sources for nucleating interfacial dislocations into each phase as shown in Figure 4 (c) and (d). Thus, the Nb layers in Cu/Nb samples have more Greens strain than the SX Nb sample. In addition, thicker Cu/Nb samples carry larger Greens stains in both Cu and Nb layers. That is because the confined layer slip (CLS) is the main dislocation activity in the SX Cu/Nb samples as shown in Figure 4 (d). The

critical stress for activating confined layer slip is inversely proportional to the layer thickness as the following [11]:

$$\tau_{CLS} = \frac{\mu b \sin\varphi}{8\pi h}\left(\frac{4-v}{1-v}\right)\ln\frac{\alpha h}{b \sin\varphi} \quad (3)$$

where h is the layer thickness, μ the shear modulus, v the Poisson's ratio, φ the angle between slip plane and the layer interface, b the Burgers vector of dislocation, and α is a coefficient representing the extent of the dislocation core. Therefore, the larger the layer thickness, the smaller the critical stress is to activate dislocation motion within the layer. The dislocation induced plasticity would increase with the layer thickness, and therefore increase the Green strain and suppress the crack propagation. In SX samples, dislocations can only come from the crack tip due to the high stress concentration, and the number of dislocation sources is limited. In contrast, the available dislocation sources are plentiful in the Cu/Nb sample due to the high density of interfacial dislocation networks [9,38]. That is why the Green strain in Cu layer in 20 nm Cu/Nb sample is even larger than that in the SX Cu sample.

3.2. POLYCRYSTALLINE SAMPLES WITH GRAIN BOUNDARIES

Figure 5 shows the atomistic structure for different PX samples at 12 % engineering strain. Figure 5 (a)-(c) present the samples for PX Cu, Cu layers in 5nm and 20 nm PX Cu/Nb samples, respectively. For PX Cu, the crack propagated within the initial grain firstly. After the tip approach the GBs, the propagation stopped and the crack was blunted at GBs as shown in Figure 5 (a). For the Cu layer in 5 nm PX Cu/Nb sample, after the preexisting crack approached the closest GBs, it continued growing along other GBs. That induced the intergranluar fracture in the thin Cu layer. However, when the layer thickness

of Cu layer increased to 20 nm, the intergranular fracture disappeared and crack also was blunted at GBs as shown in Figure 5 (c).

Figure 5 (d)-(f) present the shape and propagation path of the crack in PX Nb, Nb layer in 5 nm and 20 nm PX Cu/Nb samples, respectively. Although cracks in all three samples propagated along the GBs, differences still exist between the PX Nb and Nb layer in the PX Cu/Nb samples. In PX Nb, multiple cracks nucleated at the GBs in front of the preexisting crack. Those newly formed cracks grow along the GBs. Once they coalesced with the preexisting crack, a long crack formed across multiple GBs. The crack in the Cu/Nb grows much slower and little or to no new cracks nucleated at the front of the preexisting crack.

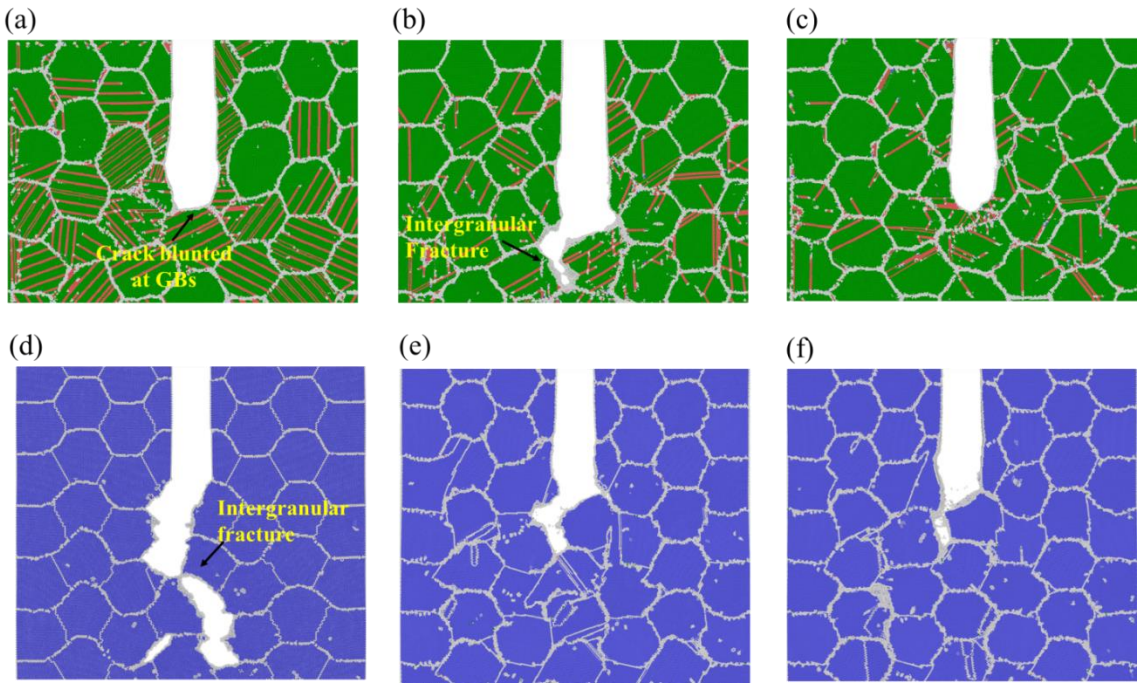

Figure 5. Atomistic structures for different PX sample at 12% strain: (a) PX Cu, (b) Cu layer in 5 nm PX Cu/Nb, (c) Cu layer in 20 nm PX Cu/Nb, (d) PX Nb, (e) Nb layer in 5 nm PX Cu/Nb; (f) Nb layer in PX 20 nm Cu/Nb.

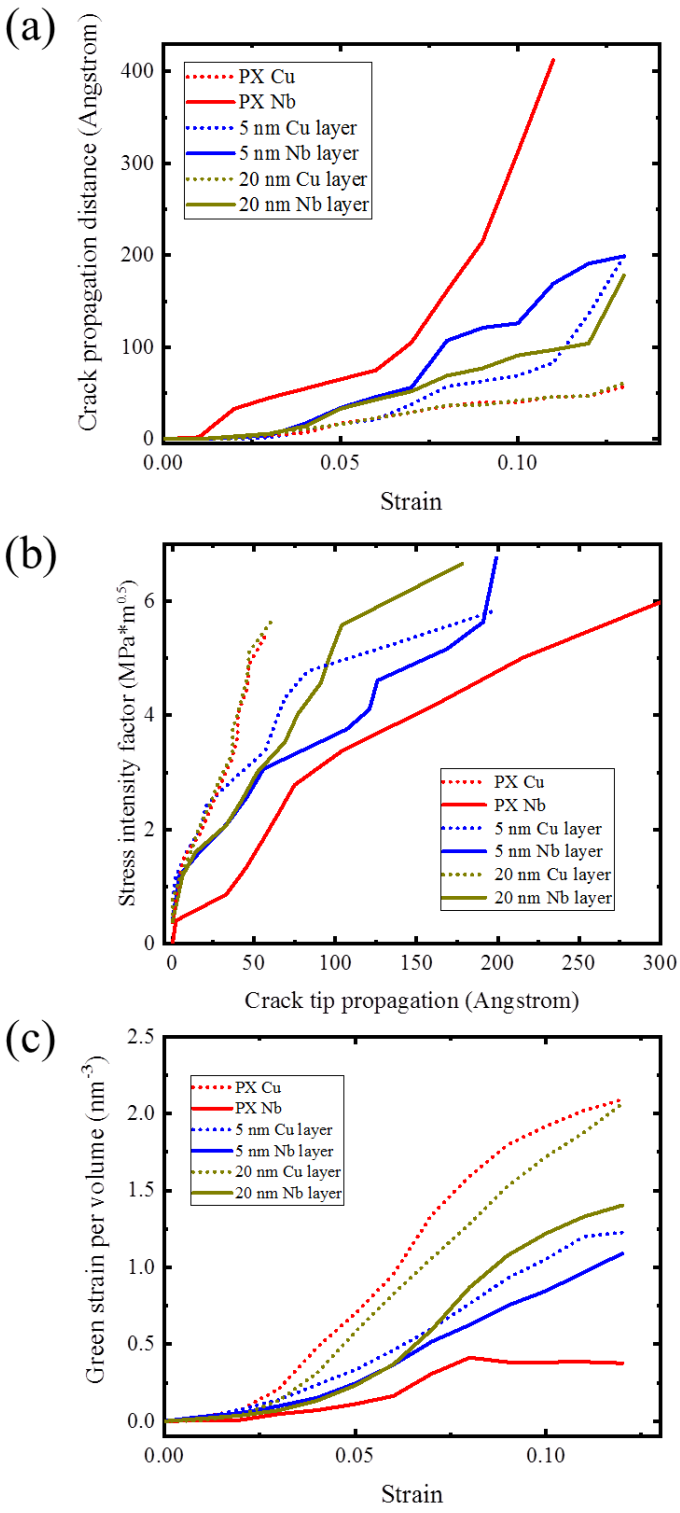

Figure 6. (a) Plot of crack propagation distance for different PX samples. (b) Stress intensity factor for different PX samples. (c) Green strain per volume for different PX samples.

Figure 6 (a) plots the crack propagation distance versus the engineering stain for all PX samples. From the plot, we can see the crack propagation process for PX Cu sample is nearly the same as that in Cu layer of 20 nm PX Cu/Nb sample. Since there was no crack blunting, the crack propagation distance in Cu layer of 5 nm PX Cu/Nb sample is much larger than the PX Cu after 6% strain. As the layer thickness increases from 5nm to 20 nm, the fracture resistance ability of Cu layer in Cu/Nb MNCs may recover to the same level as single phase PX Cu sample. Figure 6 (a) also indicates that the trend of crack propagation distance for PX Nb and Nb layer in PX Cu/Nb samples is similar to that in SX samples: i) introducing the Cu/Nb interface improved the fracture resistance of the Nb layer, ii) the thicker the layers, the better the crack resistance is. Figure 6 (b) shows the fracture toughness curves for all PX samples. We can see that, at the same crack tip propagation distance, the value of SIFs in the 20 nm Cu layer and single phase PX Cu are the same, both of which are larger than the SIF in 5 nm Cu layer. For Nb, the SIF of 5 nm Nb layer is the lowest one among the three cases. The SIF curves for 20 nm Nb and PX Nb overlap each other for the first 50 Å. After the crack propagated 50 Å, the SIF curve of 20 nm Nb deviated from the PX Nb curve. That means the Cu/Nb interface suppressed the crack propagation and increased the SIF in the 20 nm Cu/Nb.

Figure 6 (c) compares the total Green strain induced in PX samples. The Green strain induced by grain boundaries atoms were not considered on this plot, as the shape, size of grains and the GBs types are exactly the same for all PX samples. It is clear that the Green strain in the PX Cu samples is always the highest one among all cases, followed by the Cu layer in 20 nm Cu/Nb sample. The single phase PX Nb displays lowest Green strain for the full range of applied strain. This trend is consistent with the crack propagation

distance plot in Figure 6 (a). Since the excess stored elastic energy can either be released by the crack propagation or dislocation slip, larger Green strains induced by the dislocation slip can suppress the crack propagation and increase the SIF. Thus, the Green strain in Nb layers bonded by the Cu/Nb interfaces are higher than that in the single phase PX Nb and increasing the layer thickness can facilitate the dislocation activities to generate more Green strain.

4. CONCLUSION

In this work, we studied the fracture resistance of single crystalline and polycrystalline Cu/Nb MNCs by using MD simulations. Our simulation results are consistent with previous experiment results, which revealed that cracks in Cu and Nb layers may exhibit different propagation paths and distances under the same external loading. Nb layer in Cu/Nb samples exhibited better fracture resistance compared with the single phase Nb samples, as the interface can provide abundant dislocation sources for plastic deformation at the crack tip that can suppress the crack propagation and increase the fracture resistance in MNCs. Compared with the single crystalline Cu samples, the Cu/Mb interface would deteriorate the fracture resistance of Cu layers when the layer thickness of Cu is below 20 nm. As the layer thickness increases to 20 nm, the Cu layers in the MNCs possess a similar fracture resistance as that in the single phase Cu samples, as the CRSS to drive the dislocation motion decrease with the increment of the layer thickness. GBs in polycrystalline Cu/Nb samples would decrease the fracture resistance of Nb layer by promoting the intergranular fracture, while the effect of interface and layer thickness on the fracture resistance of MNCs will not be altered by the GBs. Our findings in this work

can provide fundamental understanding of the fracture behavior of MNCs and have implications for the design of nanostructured materials with better fracture resistance.

ACKNOWLEDGMENTS

This work was supported by the grants from NSF CAREER Award (CMMI-1652662). The supercomputer time allocation for completing the atomistic simulations was provided by the Extreme Science and Engineering Discovery Environment (XSEDE), award number DMR170093.

REFERENCES

1 Höchbauer, T., Misra, A., Hattar, K. & Hoagland, R. Influence of interfaces on the storage of ion-implanted He in multilayered metallic composites. Journal of applied physics 98, 123516 (2005).

2 Misra, A., Hirth, J., Hoagland, R., Embury, J. & Kung, H. Dislocation mechanisms and symmetric slip in rolled nano-scale metallic multilayers. Acta materialia 52, 2387-2394 (2004).

3 Wang, Y.-C., Misra, A. & Hoagland, R. Fatigue properties of nanoscale Cu/Nb multilayers. Scripta materialia 54, 1593-1598 (2006).

4 Misra, A., Demkowicz, M., Zhang, X. & Hoagland, R. The radiation damage tolerance of ultra-high strength nanolayered composites. Jom 59, 62-65 (2007).

5 Shao, S. & Medyanik, S. N. Interaction of dislocations with incoherent interfaces in nanoscale FCC–BCC metallic bi-layers. Modelling and Simulation in Materials Science and Engineering 18, 055010 (2010).

6 Shao, S., Zbib, H. M., Mastorakos, I. & Bahr, D. F. Effect of Interfaces in the Work Hardening of Nanoscale Multilayer Metallic Composites During Nanoindentation: A Molecular Dynamics Investigation. Journal of Engineering Materials and Technology 135, 021001-021001-021008, doi:10.1115/1.4023672 (2013).

7 Hoagland, R. G., Kurtz, R. J. & Henager Jr, C. Slip resistance of interfaces and the strength of metallic multilayer composites. Scripta materialia 50, 775-779 (2004).

8 Mastorakos, I., Abdolrahim, N. & Zbib, H. Deformation mechanisms in composite nano-layered metallic and nanowire structures. International Journal of Mechanical Sciences 52, 295-302 (2010).

9 Shao, S., Wang, J., Beyerlein, I. J. & Misra, A. Glide dislocation nucleation from dislocation nodes at semi-coherent {111} Cu–Ni interfaces. Acta Materialia 98, 206-220, doi:https://doi.org/10.1016/j.actamat.2015.07.044 (2015).

10 Misra, A., Hirth, J. & Kung, H. Single-dislocation-based strengthening mechanisms in nanoscale metallic multilayers. Philosophical Magazine A 82, 2935-2951 (2002).

11 Misra, A., Hirth, J. & Hoagland, R. Length-scale-dependent deformation mechanisms in incoherent metallic multilayered composites. Acta materialia 53, 4817-4824 (2005).

12 Huang, S., Beyerlein, I. J. & Zhou, C. Nanograin size effects on the strength of biphase nanolayered composites. Scientific Reports 7, 11251 (2017).

13 Huang, S., Wang, J. & Zhou, C. Effect of plastic incompatibility on the strain hardening behavior of Al–TiN nanolayered composites. Materials Science and Engineering: A 636, 430-433 (2015).

14 Kavarana, F., Ravichandran, K. & Sahay, S. Nanoscale steel-brass multilayer laminates made by cold rolling: microstructure and tensile properties. Scripta materialia 42, 947-954 (2000).

15 Zhu, X. F., Li, Y. P., Zhang, G. P., Tan, J. & Liu, Y. Understanding nanoscale damage at a crack tip of multilayered metallic composites. Applied Physics Letters 92, 1 (2008).

16 Zhang, J. Y. et al. Length-scale-dependent deformation and fracture behavior of Cu/ (= Nb, Zr) multilayers: The constraining effects of the ductile phase on the brittle phase. Acta Materialia 59, 7368-7379 (2011).

17 Liang, F., Tan, H. F., Zhang, B. & Zhang, G. P. Maximizing necking-delayed fracture of sandwich-structured Ni/Cu/Ni composites. Scripta Materialia 134, 28-32 (2017).

18 Hattar, K. et al. Direct Observation of Crack Propagation in Copper–Niobium Multilayers. Journal of Engineering Materials & Technology 134, 021014 (2012).

19 Farkas, D. Fracture Resistance of Nanocrystalline Ni. Metallurgical & Materials Transactions A 38, 2168-2173 (2007).

20 Zeng, Z., Li, X., Lu, L. & Zhu, T. Fracture in a thin film of nanotwinned copper. Acta Materialia 98, 313-317 (2015).

21 Zhou, X., Li, X. & Chen, C. Atomistic mechanisms of fatigue in nanotwinned metals. Acta Materialia 99, 77-86 (2015).

22 Plimpton, S. Fast Parallel Algorithms for Short-Range Molecular Dynamics. Journal of Computational Physics 117, 1-19, doi:https://doi.org/10.1006/jcph.1995.1039 (1995).

23 Liang, Z., Enrique, M., Alfredo, C., Xiang-Yang, L. & Michael, J. D. Liquid-phase thermodynamics and structures in the Cu–Nb binary system. Modelling and Simulation in Materials Science and Engineering 21, 025005 (2013).

24 Honeycutt, J. D. & Andersen, H. C. Molecular dynamics study of melting and freezing of small Lennard-Jones clusters. The Journal of Physical Chemistry 91, 4950-4963, doi:10.1021/j100303a014 (1987).

25 Mastorakos, I. N., Bellou, A., Bahr, D. F. & Zbib, H. M. Size-dependent strength in nanolaminate metallic systems. Journal of Materials Research 26, 1179-1187 (2011).

26 Abdolrahim, N., Zbib, H. M. & Bahr, D. F. Multiscale modeling and simulation of deformation in nanoscale metallic multilayer systems. International journal of plasticity 52, 33-50 (2014).

27 Martínez, E., Caro, A. & Beyerlein, I. J. Atomistic modeling of defect-induced plasticity in CuNb nanocomposites. Physical review b 90, 054103 (2014).

28 Zhou, J., Averback, R. & Bellon, P. Stability and amorphization of Cu–Nb interfaces during severe plastic deformation: Molecular dynamics simulations of simple shear. Acta Materialia 73, 116-127 (2014).

29 Misra, A. & Krug, H. Deformation behavior of nanostructured metallic multilayers. Advanced Engineering Materials 3, 217-222 (2001).

30 Hoagland, R. G., Kurtz, R. J. & Henager, C. H. Slip resistance of interfaces and the strength of metallic multilayer composites. Scripta Materialia 50, 775-779, doi:https://doi.org/10.1016/j.scriptamat.2003.11.059 (2004).

31 Schiøtz, J., Vegge, T., Di Tolla, F. D. & Jacobsen, K. W. Atomic-scale simulations of the mechanical deformation of nanocrystalline metals. Physical Review B 60, 11971-11983, doi:10.1103/PhysRevB.60.11971 (1999).

32 Hoover, W. G. Constant-pressure equations of motion. Physical Review A 34, 2499-2500, doi:10.1103/PhysRevA.34.2499 (1986).

33 Nosé, S. A unified formulation of the constant temperature molecular dynamics methods. Journal of Chemical Physics 81, 511-519 (1984).

34 Zimmerman, J. A., Bammann, D. J. & Gao, H. Deformation gradients for continuum mechanical analysis of atomistic simulations. International Journal of Solids and Structures 46, 238-253 (2009).

35 Stukowski, A., Bulatov, V. V. & Arsenlis, A. Automated identification and indexing of dislocations in crystal interfaces. Modelling and Simulation in Materials Science and Engineering 20, 085007 (2012).

36 Stukowski, A. Visualization and analysis of atomistic simulation data with OVITO–the Open Visualization Tool. Modelling and Simulation in Materials Science and Engineering 18, 015012 (2009).

37 Zhang, Y., Tucker, G. J. & Trelewicz, J. R. Stress-assisted grain growth in nanocrystalline metals: Grain boundary mediated mechanisms and stabilization through alloying. Acta Materialia 131, 39-47 (2017).

38 Shao, S., Wang, J., Misra, A. & Hoagland, R. G. Spiral Patterns of Dislocations at Nodes in (111) Semi-coherent FCC Interfaces. Scientific Reports 3, 2448, doi:10.1038/srep02448

III. EFFECT OF PLASTIC INCOMPATIBILITY ON THE STRAIN HARDENING BEHAVIOR OF AL-TIN NANOLAYERED COMPOSITES

Sixie Huang[1], Jian Wang[2] and Caizhi Zhou[1]

[1]Deparment of Materials Science and Engineering,
Missour University of Science and Technology, Rolla, MO 65409, USA

[2]Materials Science and Technology Division,
Los Alamos National Laboratory, Los Alamos, NM 87545, USA

Published in Materials Science and Engineering: A, 636: 430-433, 2015

ABSTRACT

The strain hardening behavior of Al-TiN nanolayered composites induced by plastic incompatibility was studied by 3-D discrete dislocation dynamics (DDD) simulations. Our simulations results indicate the strain hardening rate solely induced by the plastic incompatibility is independent of layer thickness and dislocation density at a constant layer thickness ratio, while the yield stress exhibits a strong size effect. Furthermore, the strain hardening rate increases with decreasing Al/TiN layer thickness ratio and our predicted results match well with prior experiment data.

Keywords: Discrete dislocation dynamics, Strain hardening, Plastic incompatibility, Nanolayered composites

1. INTRODUCTION

Metal-ceramic nanolayered composites (MCNCs) which composed of alternating metal and ceramic layers at nanoscale have attracted much attention in the materials science community due to their promising mechanical, physical, and chemical properties [1-6]. These

new advanced materials are practically useful for harsh environments and extreme loading and can lead to new performance levels not achievable with current materials [7,8].

Recently, several experiment groups have performed micro-compression testing on MCNCs to study their mechanical response under uniaxial compressive stress. Lotfian at al.[9] investigated the influence of temperatures on the mechanical behavior of SiC/Al MCNCs and found that the composites presented a very high strain hardening rate at 23°C, while the hardening rate decreased dramatically at 100˚C. In addition, plastic deformation of Al layers was constrained by SiC layers at 23˚C while massive extrusion of the Al out of pillars was observed at 100˚C. Singh at al.[10] did fractographic analysis of the compressed pillars and claimed that the mutual constraint between the hard and soft layers was thought responsible for the very high strengths. For Al-TiN nanolayered composites, Bhattacharyya at al.[1] revealed that the high strengths were layer thickness dependent and accompanied by ultrahigh strain-hardening rates. Besides that, their cross-sectional transmission electron microscopy observations indicated that few dislocation pileups formed in Al layers that can prevent the concentration of stresses and thus enhance the uniform deformation of the TiN layers [11]. Li at al. [12] revealed a profound size effect on the mechanical deformation of Al-TiN nanolayered composites, i.e., significant plastic co-deformation is only observed when the layer thickness is reduced to a few nanometers. For Cu/PdSi multilayered composites with layer thicknesses ranging from 10 to 120 nm, Knorr at al.[13] found both Cu and PdSi layers co-deform without delamination, rupture, cracking or localized shear up to 85% plastic strains.

Most prior experiment studies demonstrated that the high strengths of MCNCs at room temperature were accompanied by ultra-high strain hardening rates that were of the

order of E/10-E/2. This extraordinarily strain hardening behavior is attributed to the plastic co-deformation in MCNCs [14], which can be rationalized as follows. Plastic deformation first commences in metal layers because of the relatively lower yield strength and higher mobility of dislocations as compared to ceramics. Dislocations glide in the metal layers confined by metal-ceramic interfaces, depositing dislocations at the interfaces. The glide dislocations from the metal layer deposited at the interfaces represent the plastic incompatibility between the two layers. Accompanying the development of plastic deformation in metals, the further nucleation and gliding of dislocations in metal layers become difficult, corresponding to strain hardening induced by plastic incompatibility. Besides this major hardening mechanism, the interactions between mobile dislocations and accumulated interfacial dislocations and the interactions between mobile dislocation dipoles also hinder the gliding of dislocations in layers. Currently, quantitative analysis of each hardening mechanism is still lack. Further work is needed to understand the underlying mechanisms that control the mechanical response of MCNCs.

3-D discrete dislocation dynamics (DDD) model is a powerful tool for exploring plastic deformation of metallic systems at both small scales and bulk sizes [15-23]. Most recent developments of 3-D DDD model were for studies of the size-effect in single crystal pillars, which is known to be induced by the limitation of available sources and the variation of dislocation source lengths at small scales. For the studies on metallic nanolayers, the two main foci are determining the stress required for a dislocation to cross an interface [24-26] and the stress required to propagate dislocations in a confined layer slip (CLS) mode [27-29]. However, 3-D DDD model has not yet been applied on the study of the mechanical response of MCNCs.

In this study, we employ 3-D DDD simulations to quantitatively analyze the effect of plastic incompatibility on the mechanical response of Al-TiN nanolayered composites under uniaxial compression. We compare our simulation results with experiment data from micro-compression testing to explore the effects of dislocation density, strain rate, layer thickness and modulus mismatch on the mechanical response of Al-TiN nanolayered composites.

2. METHODS

The 3-D DDD framework described in ref. [30,31] has been used in this study to simulate the mechanical response of Al–TiN nanolayered composites under uniaxial compression. A bilayer model composed of Al and TiN layers is adopted with periodic boundary condition in all three directions. According to the experiment results[1], the *x*, *y* and *z* directions of the simulation box correspond to $[11\bar{2}]$, $[1\bar{1}0]$ and $[111]$ directions in the Al phase, respectively. The lengths of the box in *x* and *y* directions are both around 1.0 μm. The uniaxial compression is applied along the *z* direction perpendicular to the interface to mimic the micro-compression experimental condition and while thickness of each phase varies in different cases.

In this study, we assume (a) the TiN layer can only be elastically deformed during the entire simulation; (b) the interface between the TiN and Al layers is strong enough to bond these two phases together, such that the Al and TiN layers will be forced to deform equally in the *x*–*y* plane. The total strain of the composite in *x* and *y* directions are $\bar{\varepsilon}_x = \varepsilon_x^{Al} = \varepsilon_x^{TiN}, \bar{\varepsilon}_y = \varepsilon_y^{Al} = \varepsilon_y^{TiN}$, and the total strain of the composite in the *z* direction can be calculated by $\bar{\varepsilon}_z = (h_{Al}\varepsilon_z^{Al} + h_{TiN}\varepsilon_z^{TiN})/(h_{Al} + h_{TiN})$, where h_{Al} and h_{TiN} are the layer

thicknesses, ε_x^{Al}, ε_y^{Al} and ε_z^{Al} are the strains in *x*, *y* and *z* directions for Al phase; ε_x^{TiN}, ε_y^{TiN} and ε_z^{TiN} are the strains for TiN phase. The compressive loading is applied along the *z* direction and this configuration stratifies an isostress condition:

$$\bar{\sigma}_x = \frac{h_{Al}\sigma_x^{Al} + h_{TiN}\sigma_x^{TiN}}{h_{Al} + h_{TiN}} = 0 \tag{1a}$$

$$\bar{\sigma}_y = \frac{h_{Al}\sigma_y^{Al} + h_{TiN}\sigma_y^{TiN}}{h_{Al} + h_{TiN}} = 0 \tag{1b}$$

$$\bar{\sigma}_z = \sigma_z^{Al} = \sigma_z^{TiN} \tag{1c}$$

where σ_x^{Al}, σ_y^{Al} and σ_z^{Al} are the stresses in *x*, *y* and *z* directions for the Al phase, and σ_x^{TiN}, σ_y^{TiN} and σ_z^{TiN} are the stress for the TiN phase. In this work, both phases are taken to be elastically isotropic and the materials properties were used: Shear modulus E_{Al} = 70 GPa, E_{TiN} = 251 GPa and Poisson's ratio υ_{Al} = 0.35, υ_{TiN} = 0.25.

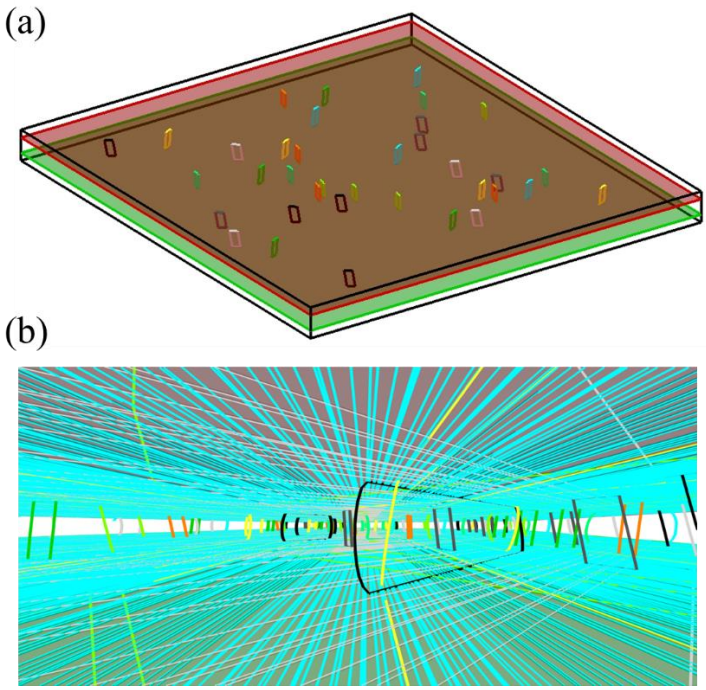

Figure 1. Dislocation structures: (a) initial; (b) 5% strain (the evolution of dislocation structure can be found in Supplemental materials)

In order to study the effect of plastic incompatibility on the mechanical response of Al-TiN nanolayered composites, the interfaces between the two phases are considered impenetrable for dislocations and the dislocation nucleation, dislocation interactions are not considered in this work.

3. RESULTS AND DISCUSSION

To explore the plastic deformation in Al layers, dislocation loops are randomly put in Al layers at the beginning of the simulation and each slip system is assigned an equal number of dislocation loops. Figure 1(a) shows an example of initial dislocation structure in the simulation box with the thicknesses of h_{Al} = 18 nm and h_{TiN} = 2 nm, respectively. A constant strain rate of -2.0×10^5 is applied along the *z* direction perpendicular to the interface. To test the effect of initial dislocation density on the simulation results, two different initial dislocation densities are used for comparison, ρ = 6.5×10^{13} m^{-2} for 36 dislocation loops and ρ = 1.3×10^{14} m^{-2} for 72 dislocation loops. Figure 2(a) shows the stress-strain curves for two different densities under the same applied strain rate together with experiment results from Al-TiN miropillar compression test [1]. It is clear that the strain hardening rates for different densities are the same and very close to that for the experimental curve inthe plastic regime. Estimated from both our simulation and experiment results, the strain hardening rate is at the order of $E_{Al}/5$ for h_{Al} = 18 nm and h_{TiN} = 2 nm composite where E_{Al} is the shear modulus of Al. This value is much higher than the strain hardening rate for bulk Al which is typical less than 500 MPa [1]. Obviously, the initial dislocation density only affects the yielding point of the stress-strain curves by raising it with fewer dislocations. However, this effect is tiny as demonstrated in Figure

2(a). Decreasing the density from 1.3×10^{14} m^{-2} to 6.5×10^{13} m^{-2} can only increase the 0.2% offset yield stress, $\sigma_{0.2\%}$, about 1.2 %.

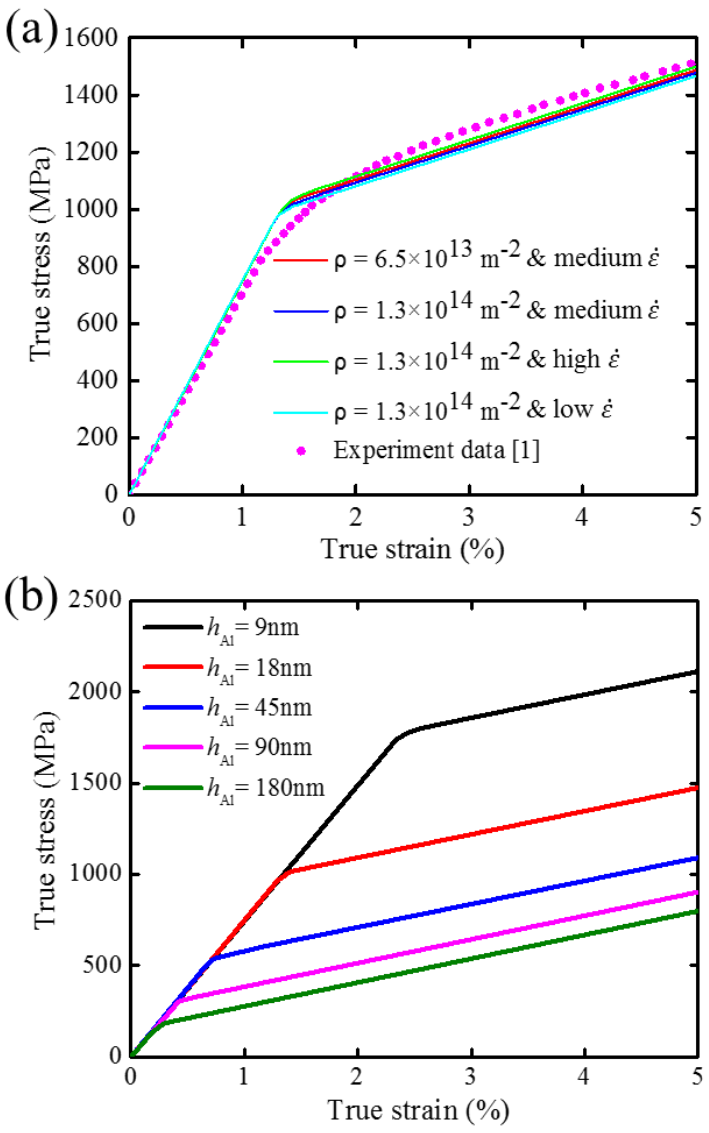

Figure 2. Stress–strain curves (a) for h_{Al} = 18nm and h_{TiN} = 2nm under different strain rates and dislocation densities, ρ, compared with experimental data (symbols); (b) different layer thicknesses with $h_{Al} : h_{TiN} = 9 : 1$.

Since the applied strain rate in this study is much higher than that used in micropillar compression testing, we also investigated the effect of applied strain rate on the

simulation results by increasing and decreasing the applied strain rate for five times to -1.0×10^{6} s^{-1} and -4.0×10^{4}, respectively. The stress-strain curves from three different applied strain rates are shown in Figure 2(a). We can see that the slope of the stress-strain curves in plastic regime is not affected by the change of the applied strain rate, although the $\sigma_{0.2\%}$ increases about 1.4 % from $\dot{\varepsilon} = -2.0\times10^{5}$ s^{-1} to $\dot{\varepsilon} = -1.0\times10^{6}$ s^{-1} and decrease about 1.8 % from $\dot{\varepsilon} = -2.0\times10^{5}$ s^{-1} to $\dot{\varepsilon} = -4.0\times10^{5}$ s^{-1}. When compared with experimental results, the 0.2% offset yield stresses for $\dot{\varepsilon} = -4.0\times10^{4}$ s^{-1}, $\dot{\varepsilon} = -2.0\times10^{5}$ s^{-1} and $\dot{\varepsilon} = -1.0\times10^{6}$ s^{-1} from our calculations are about only 1.6 %, 2.2 % and 3.6% larger than that from micropillar compression test, respectively. Thus, the high applied strain rate in this study is not critical for the mechanical response of Al-TiN nanolayered composites.

In this study, the ultra-high strain hardening rate in Al-TiN nanolayered composites is solely induced by the plastic incompatibility between the Al layer and TiN layer. After yielding, the motion of dislocations in the Al layer generates plastic strain to make the Al layer expanded in the *x*-*y* plane, while the TiN layer does not yield and is still under elastic deformation at that time. As the interface is strong enough to force Al and TiN layers to deform equally in the *x*–*y* plane, the Al layer will experience compressive stress exerted from the TiN layer to constrain its in-plane expansion. This compressive stress on Al layers will slow down the motion of dislocations and induce strain hardening effect on the whole sample. Although this strain hardening effect induced by the plastic incompatibility between metallic and ceramic layers has already been mentioned in several studies [22,26,27], our work is the first time, to the best of our knowledge, quantitatively analyzing this strain hardening effect isolatedly.

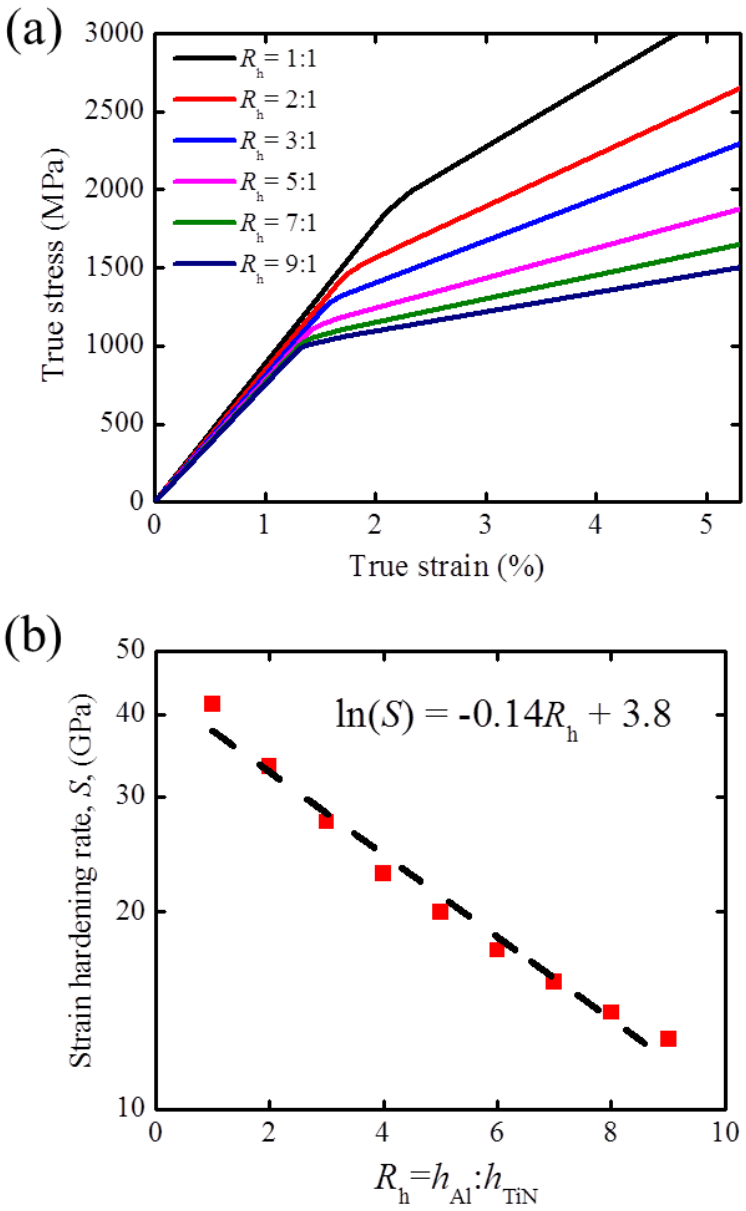

Figure 3. Stress-strain curves for different R_h with h_{Al} = 18nm; (b) strain hardening rates, S, vs. layer thickness ratio, R_h.

To understand how strain hardening could be influenced by the variation of layer thicknesses, we performed a series of simulations for different layer thicknesses with a constant layer thickness ratio, $R_h = h_{Al}:h_{TiN}$, at 9:1. All these simulations are under the same applied strain rate of -2.0×10^5 $s^{-1}$and with the same initial dislocation density at

1.3×10^{14} m^{-2}. The stress-strain curves are shown in Figure 2(b). It is interesting that, regardless of layer thickness, all the slopes of the stress-strain curves in plastic regime are almost the same at the order of $E_{Al}/5$, while the yield stress increases with decreasing layer thickness. Results of this comparison suggest that the strain hardening behavior solely induced the plastic incompatibility is independent of the layer thickness at a constant layer thickness ratio. According to equations (1a) and (1b), the magnitude of the compressive stress, $\sigma^{Al}_{x\ or\ y}$ is proportional to $\frac{h_{TiN}}{h_{Al}}$. If the thicknesses of Al and TiN decrease at the same time with a constant thickness ratio, the magnitude of in-plane compressive stress on Al layers will not change. Thus, the strain hardening rate will not change with the thickness itself, but with the thickness ratio. It is worth to mentioning that there are no slip activity parallel to the interface in this study, which may affect the strain hardening behavior by intersecting the mobile dislocations. However, the dislocation interactions are not considered in this work. Thus, the simulation results will not change with or without slip activities parallel to the interface.

According to the rule-of-mixtures, the elastic modulus of Al-TiN nanolayered composites will increase with the volume fraction of the TiN phase, as the modulus of the TiN phase is much higher than that for the Al phase. However, the influence of the volume fraction (or layer thickness ratio in this study) on the plastic behavior of Al-TiN nanolayered composites is still unclear. To gain insight on how strong the influence of layer thickness ratio is on the strain hardening behavior, we repeated the simulations for various R_h from 1:1 to 9:1 at a constant Al layer thickness of 18 nm. Figure 3 (a) compares the stress-strain curves for these cases and Figure 3(b) plots the strain hardening rate vs. the layer thickness ratio. We observe that the predicted strain hardening rate in plastic

regime increases with the volume fraction of TiN phase. This trend follows prior experimental results from Al-TiN micropillar compression testing [1]. More interestingly, our predicted strain hardening rates for R_h = 1:1 and 9:1 match well with the values from micropillar compression test which are $E_{Al}/2$ and $E_{Al}/5$, respectively. In addition, we found that our predicted strain hardening rate can be fitted by $\ln(S) = -0.14R_h + 3.8$, where S is the strain hardening rate and R_h is the layer thickness ratio.

Although we idealize the interface by assuming it is strong enough to force Al and TiN layers to deform equally in the *x*–*y* plane, this basic assumption is not contrary to the experiment observations. In actual Al-TiN micropillar compression test [1], no extrusion of the Al layers at the edges of the pillar was observed at room temperature even with the total strain larger than 10%. That means the interface is strong enough to bond these two phases together, which supports our basic assumption. We also need to emphasize that the TiN layer is assumed to be deformed elastically, and this study only investigates the strain hardening behavior of Al-TiN nanolayered composites with layers thickness above 5nm. Although the plastic deformation of the TiN layer is observed at 5 nm and below in Ref. 12, it will not affect our basic assumption here, since the experiment in Ref. 12 also confirmed that the plastic deformation in TiN was suppressed above 5 nm.

In making comparisons of our simulation results with experimental curves, it should be mentioned that the transition from elastic to plastic regime of the experiment curves is smoother than those from our simulations, even though the strain hardening rates from our calculations match well with experiment results. There are two major factors not considered in this study that may cause this difference: dislocation interaction and dislocation nucleation from the interface. While the calculation of dislocation nucleation

and interactions need more time and effort, especially for the interactions between dislocations in the Al phase and dislocations on the interface. That is out of the scope of this study. Wang et al. [8,14] recently analyzed the effect of dislocation nucleation on the plastic deformation in MCNCs. They found that, even before yielding, the nucleation can still occur and generate a certain amount of plastic deformation before plastic flow, thus the flow stress can be reduced slightly.

4. CONCLUSIONS

In summary, 3-D DDD simulations was used in this study to explore the effect of plastic incompatibility on the strain hardening behavior of Al-TiN nanolayered composites. Our simulations results indicate that the strain hardening rate of Al-TiN nanolayered composites is independent of layer thickness and dislocation density at a constant layer thickness ratio, while the yield stress shows a strong size-dependent behavior. Furthermore, the strain hardening rate increases with decreasing the h_{Al}:h_{TiN} ratio and our predicted results match well with prior experiment data. Although a great simplification has been made in our model, the results from this study can still shed light on the role of dislocation mechanisms in the mechanical response of MCNCs.

ACKNOWLEDGEMENTS

SH and CZ gratefully acknowledge financial support from The University of Missouri Research Board and MRC at Missouri University of Science and Technology.

REFERENCES

1 Bhattacharyya, D., Mara, N., Dickerson, P., Hoagland, R. & Misra, A. Compressive flow behavior of Al–TiN multilayers at nanometer scale layer thickness. Acta Materialia 59, 3804-3816 (2011).

2 García-García, A. et al. Magnetic properties of Fe⁄ MgO granular multilayers prepared by pulsed laser deposition. Journal of Applied Physics 105, 063909 (2009).

3 Jiménez-Villacorta, F., Espinosa, A., Céspedes, E. & Prieto, C. Magnetic properties and short-range structure analysis of granular cobalt silicon nitride multilayers. Journal of Applied Physics 110, 113909 (2011).

4 Zhang, Q.-C. Optimizing analysis of W-AlN cermet solar absorbing coatings. Journal of Physics D: Applied Physics 34, 3113 (2001).

5 Zhao, S. & Wäckelgård, E. Optimization of solar absorbing three-layer coatings. Solar energy materials and solar cells 90, 243-261 (2006).

6 Chance, D. A. & Wilcox, D. L. Metal-ceramic constraints for multilayer electronic packages. Proceedings of the IEEE 59, 1455-1462 (1971).

7 Sinnott, S. B. & Dickey, E. C. Ceramic/metal interface structures and their relationship to atomic-and meso-scale properties. Materials Science and Engineering: R: Reports 43, 1-59 (2003).

8 Salehinia, I., Shao, S., Wang, J. & Zbib, H. Plastic deformation of metal/ceramic nanolayered composites. JOM 66, 2078-2085 (2014).

9 Lotfian, S. et al. High temperature micropillar compression of Al/SiC nanolaminates. Acta Materialia 61, 4439-4451 (2013).

10 Singh, D., Chawla, N., Tang, G. & Shen, Y.-L. Micropillar compression of Al/SiC nanolaminates. Acta Materialia 58, 6628-6636 (2010).

11 Bhattacharyya, D., Mara, N. A., Dickerson, P., Hoagland, R. & Misra, A. A transmission electron microscopy study of the deformation behavior underneath nanoindents in nanoscale Al–TiN multilayered composites. Philosophical Magazine 90, 1711-1724 (2010).

12 Li, N., Wang, H., Misra, A. & Wang, J. In situ Nanoindentation Study of Plastic Co-deformation in Al-TiN Nanocomposites. Scientific Reports 4, 6633, doi:10.1038/srep06633 (2014).

13 Knorr, I., Cordero, N., Lilleodden, E. T. & Volkert, C. A. Mechanical behavior of nanoscale Cu/PdSi multilayers. Acta Materialia 61, 4984-4995 (2013).

14 Wang, J. & Misra, A. Strain hardening in nanolayered thin films. Current Opinion in Solid State and Materials Science 18, 19-28 (2014).

15 Akarapu, S., Zbib, H. & Bahr, D. Analysis of heterogeneous deformation and dislocation dynamics in single crystal micropillars under compression. International Journal of Plasticity 26, 239-257 (2010).

16 Balint, D., Deshpande, V., Needleman, A. & Van der Giessen, E. Size effects in uniaxial deformation of single and polycrystals: a discrete dislocation plasticity analysis. Modelling and Simulation in Materials Science and Engineering 14, 409 (2006).

17 Benzerga, A. & Shaver, N. Scale dependence of mechanical properties of single crystals under uniform deformation. Scripta materialia 54, 1937-1941 (2006).

18 Devincre, B., Kubin, L. & Hoc, T. Physical analyses of crystal plasticity by DD simulations. Scripta Materialia 54, 741-746 (2006).

19 Ghoniem, N., Tong, S.-H. & Sun, L. Parametric dislocation dynamics: a thermodynamics-based approach to investigations of mesoscopic plastic deformation. Physical Review B 61, 913 (2000).

20 Shao, S., Abdolrahim, N., Bahr, D. F., Lin, G. & Zbib, H. M. Stochastic effects in plasticity in small volumes. International Journal of Plasticity 52, 117-132 (2014).

21 Zhou, C., Beyerlein, I. J. & LeSar, R. Plastic deformation mechanisms of fcc single crystals at small scales. Acta Materialia 59, 7673-7682 (2011).

22 Zhou, C., Biner, S. & LeSar, R. Simulations of the effect of surface coatings on plasticity at small scales. Scripta Materialia 63, 1096-1099 (2010).

23 Zhou, C., Biner, S. B. & LeSar, R. Discrete dislocation dynamics simulations of plasticity at small scales. Acta Materialia 58, 1565-1577, doi:http://dx.doi.org/10.1016/j.actamat.2009.11.001 (2010).

24 Ghoniem, N. M. & Han, X. Dislocation motion in anisotropic multilayer materials. Philosophical Magazine 85, 2809-2830 (2005).

25 Han, X. & Ghoniem, N. M. Stress field and interaction forces of dislocations in anisotropic multilayer thin films. Philosophical Magazine 85, 1205-1225 (2005).

26 Shehadeh, M., Lu, G., Banerjee, S., Kioussis, N. & Ghoniem, N. Dislocation transmission across the Cu/Ni interface: a hybrid atomistic–continuum study. Philosophical Magazine 87, 1513-1529 (2007).

27 Akasheh, F., Zbib, H., Hirth, J., Hoagland, R. & Misra, A. Dislocation dynamics analysis of dislocation intersections in nanoscale metallic multilayered composites. Journal of applied physics 101, 084314 (2007).

28 Akasheh, F., Zbib, H., Hirth, J., Hoagland, R. & Misra, A. Interactions between glide dislocations and parallel interfacial dislocations in nanoscale strained layers. Journal of Applied Physics 102, 034314 (2007).

29 Zbib, H. M., Overman, C. T., Akasheh, F. & Bahr, D. Analysis of plastic deformation in nanoscale metallic multilayers with coherent and incoherent interfaces. International Journal of Plasticity 27, 1618-1639 (2011).

30 Wang, J., Zhou, C., Beyerlein, I. J. & Shao, S. Modeling interface-dominated mechanical behavior of nanolayered crystalline composites. Jom 66, 102-113 (2014).

31 Wang, Z., Ghoniem, N., Swaminarayan, S. & Lesar, R. A parallel algorithm for 3D dislocation dynamics. Journal of Computational Physics 219, 608-621 (2006).

SECTION

4. CONCLUSIONS AND FUTURE WORKS

4.1. CONCLUSIONS

Atomistic simulations, such as Molecular Dynamics (MD) simulations, can shed light onto the deformation and failure mechanisms of Nanocrystalline (NC) materials by evaluating the underlying atomic scale processes of deformation and fracture. With the input parameters from atomistic simulations, 3-Dimentional (3-D) Discrete Dislocation Dynamics (DDD) can be used to explore plastic deformation of metallic systems at both the nano and micro-scales. In this research, both the MD and the 3-D DDD were used to study the deformation of Metallic Nanolayered Composites (MNCs) or Metal-Ceramic Nanolayered Composites (MCNCs) and explore the effect of the interface and grain boundaries on mechanical properties.

In paper one, MD simulations were applied to investigate the microstructural size scaling on the strength of NC MNCs Cu/Nb composites. Scaling effects on both the intralayer NC grain size d and layer thickness h were investigated. The calculations revealed strongly coupled d-h effects. Unlike single crystalline MNCs without grain boundaries, where plasticity is initiated by emission of dislocations from the interfaces preferentially into one of the phases, in polycrystalline MNCs dislocations are emitted from the junctions between grain boundaries and interfaces. Therefore, both phases participate in yield and plastic flow in polycrystalline MNCs. Further, the grain size d controls the yield phenomenon, with the finest of grain sizes $d \leq 5$ nm yielding via intralayer Gain Boundary Sliding (GBS), and larger grain sizes $d > 5$ nm yielding by intralayer Grain

Boundary dislocation Emission (GBE). Last, the grain size *d* also affects the sensitivity of NC MNCs strength to reductions in *h.* Partial dislocation activity occurs when GBS dominates and the effect of *h* on strength is weak, whereas full dislocation activity prevails when GBS is small (< 60%) and the smaller the amount of GBS the greater the gains in strength with reduction in *h.* The grains should be as large as possible to improve the strengthening benefits of reductions in layer thickness. In most cases, the grain size of MNCs with different *h* are not reported or are not the same. These findings help to better interpret *h*-scale effects on measured yield or flow strength.

In paper two, an atomistic simulation was applied to study the fracture resistance behavior of Cu/Nb MNCs. The effects of the interface, the layer thickness, and grain boundaries were investigated. Results show that Cu and Nb layers have different crack propagation paths and distances, consistent with the previous experimental work. Compared with single phase Nb samples, the interfaces can increase the fracture resistance of Nb layers by promoting interfacial nucleation of dislocations and creating uniform plastic deformation. In contrast to single-phase Cu samples, the interface decreases the fracture resistance of Cu layers when the layer thickness is small (< 10 nm). The fracture resistance of both layers would benefit by a thicker sample. When the layer thickness increases to 20 nm the Cu layers in the MNCs have a similar fracture resistance to single-phase Cu samples because the critical resolved shear stress to drive dislocation motion decreases with the layer thickness. The introduction of GBs would decrease the fracture resistance of the Nb layer by promoting intergranular fracture but does not alter the effect of interfaces and the layer thickness. These findings provide the basic information for

understanding the mechanics of MNCs and have implications for the design of materials with better fracture resistance.

In paper three, an atomistic-informed dislocation dynamics model was developed to study Al-TiN nanolayered composites. As the TiN layers can only be elastically deformed during the simulation, this model simplifies the work for investigating the plastic incompatibility between two layers. The interfacial nucleation of dislocations was not considered in the model since the TiN is a ceramic layer. The simulated results indicated that the strain hardening rate of Al–TiN nanolayered composites is independent of the layer thickness and the dislocation density at a constant layer thickness ratio. Furthermore, the strain hardening rate increases with a decreasing h_{Al} :h_{TiN} ratio and the predicted results match well with the prior experimental data.

4.2. FUTURE WORKS

The critical grain size of Cu/Nb MNCs for the strength in this study is 5 nm. It is of interest to explore why the critical grain size is 5 nm by additional atomistic modeling works. In the future, atomistic simulations will be applied to study the Critical Resolved Shear Stress (CRSS) for a dislocation to glide in the Cu and Nb phase of Cu/Nb MNCs and the CRSS for a tilt grain boundary sliding. Nanolayered composites with the same metallic phase in each layer, e.g. Cu/Cu, but different crystallographic orientation relationships, e.g. the interface normal is {111} for the first layer and {110} for the second layer, will be created and studied by the MD simulation. The initial atomistic structure for Cu/Nb MNCs in this study follow the experimental samples fabricated by a PVD method. Since the ARB processes produce the Cu/Nb MNCs in a bulk form, which is more commercially viable to

production, it is of interest to study Cu/Nb MNCs follow the crystallographic orientation relationship in ARB production.

The dislocation dynamics model in this study is a simplified version and only works for the MCNCs. In the future, a modified dislocation dynamics model for MNCs will be developed. In the updated model, the behavior of the dislocation in the second layer will be considered. Based on the results from atomistic simulation, the interfacial misfit dislocation network, the CRSS for the nucleation of interfacial dislocation and the CRSS for the nucleation of dislocation from grain boundaries should be considered in the updated dislocation dynamics model. Finally, the new dislocation dynamics model will be applied to study Cu/Nb MNCs.

APPENDIX

A FORTRAN CODE TO GENERATE THE POLYCRYSTALLINE STRUCTURE BASED ON VORONOI ALGORITHM.

```
Xl=400.0; Yl=346.0; ZL=150.0; NANG=4
XLHALF = XL/2.0; YLHALF = YL/2.0; ZLHALF = ZL/2.D0
RDG(1,1)=0.1*XL;  RDG(2,1)=0.333*YL; RDG(3,1)=0.01
RDG(1,2)=0.6*XL;  RDG(2,2)=0.333*YL; RDG(3,2)=0.01
RDG(1,3)=0.35*XL; RDG(2,3)=0.866*YL; RDG(3,3)=0.01
RDG(1,4)=0.85*XL; RDG(2,4)=0.866*YL; RDG(3,4)=0.01

        DO I=1, NANG
                if(i==1)THETAI=0
                if(i==2)THETAI=Pi/6.0
                if(i==3)THETAI=Pi/2.0
                if(i==4)THETAI=Pi/3.0
                xx=0.0;yy=0.0;zz=1.0
                R11(I) =  cos(THETAI)+xx*xx*(1-cos(THETAI));
                R21(I) = xx*yy*(1-cos(THETAI))-zz*sin(THETAI);
                R31(I) =  xx*zz*(1-cos(THETAI))+yy*sin(THETAI) ;
                R12(I) =  xx*yy*(1-cos(THETAI))+zz*sin(THETAI);
                R22(I) = cos(THETAI)+yy*yy*(1-cos(THETAI));
                R32(I) =  zz*yy*(1-cos(THETAI))-xx*sin(THETAI) ;
                R13(I) =  xx*zz*(1-cos(THETAI))-yy*sin(THETAI) ;
                R23(I) = zz*yy*(1-cos(THETAI))+xx*sin(THETAI);
                R33(I) =  cos(THETAI)+zz*zz*(1-cos(THETAI))  ;
        ENDDO
alat=3.615000 ! lattice parameters.
RLIST = alat*SQRT(2.0D0)/2.D0*0.75d0; Ncell = 4; ntype(1:4) = 1
BASIS(1:3,1) = ZERO; BASIS(1:3,2:4) = HALF; BASIS(1,2) = ZERO
BASIS(2,3) = ZERO; BASIS(3,4) = ZERO; SHFFT(1:3) = QUAR; I = 1
        DO IGRAIN =1, NANG
        DO IBASIS =1, NCELL
                ZLOOP:      DO IZ=-90, 90
                YLOOP:      DO IY=-90, 90
                XLOOP:       DO IX=-90, 90
       N(1:3) = (/IX,IY,IZ/)
      RDD(1:3) = BASIS(1:3,IBASIS) + MATMUL(aunit,N)
        RDD1(i)=RDD(1);RDD2(i)=RDD(2);RDD3(i)=RDD(3);
          Rd1(I) = RDG(1,IGRAIN)+&
alat*(R11(IGRAIN)*RDD1(I)+R12(IGRAIN)*RDD2(I)+R13(IGRAIN)*RDD3(I))
        Rd2(I) = RDG(2,IGRAIN)+ &
alat*(R21(IGRAIN)*RDD1(I)+R22(IGRAIN)*RDD2(I)+R23(IGRAIN)*RDD3(I))
```

```
          Rd3(I) = RDG(3,IGRAIN)+ &
alat*(R31(IGRAIN)*RDD1(I)+R32(IGRAIN)*RDD2(I)+R33(IGRAIN)*RDD3(I))
  IF(Rd3(I).GT.(ZL-0.5).OR.Rd3(I)<0.5) CYCLE XLOOP
         DX = Rd1(I)-RDG(1,IGRAIN); DY = Rd2(I)-RDG(2,IGRAIN)
         DZ = Rd3(I)-RDG(3,IGRAIN); GDC = SQRT(DX**2+DY**2)
IIGRAIN_LOOP:DO IIGRAIN = 1, NANG
        IF(IGRAIN.EQ.IIGRAIN) CYCLE IIGRAIN_LOOP
        DX = Rd1(I)-RDG(1,IIGRAIN); DY = Rd2(I)-RDG(2,IIGRAIN)
        DZ = Rd3(I)-RDG(3,IIGRAIN)
IF(DX.GT.XLHALF) DX=DX-XL; IF(DX.LT.-XLHALF) DX=DX+XL
IF(DY.GT.YLHALF) DY=DY-YL; IF(DY.LT.-YLHALF) DY=DY+YL
        GD = SQRT(DX**2+DY**2)
        IF (GD.LT.(GDC))CYCLE XLOOP
           ENDDO IIGRAIN_LOOP
          atype(i)=1; I = I + 1
                              ENDDO XLOOP
                              ENDDO YLOOP
                             ENDDO ZLOOP
          ENDDO
          ENDDO
       NAN = I-1
```

BIBLIOGRAPHY

1 Höchbauer, T., Misra, A., Hattar, K. & Hoagland, R. Influence of interfaces on the storage of ion-implanted He in multilayered metallic composites. Journal of applied physics 98, 123516 (2005).

2 Misra, A., Hirth, J., Hoagland, R., Embury, J. & Kung, H. Dislocation mechanisms and symmetric slip in rolled nano-scale metallic multilayers. Acta materialia 52, 2387-2394 (2004).

3 Wang, Y.-C., Misra, A. & Hoagland, R. Fatigue properties of nanoscale Cu/Nb multilayers. Scripta materialia 54, 1593-1598 (2006).

4 Misra, A., Demkowicz, M., Zhang, X. & Hoagland, R. The radiation damage tolerance of ultra-high strength nanolayered composites. Jom 59, 62-65 (2007).

5 Garcia-Mateo, C., FG, C. & HKDH, B. Development of hard bainite. ISIJ international 43, 1238-1243 (2003).

6 Beyerlein, I. J. et al. Emergence of stable interfaces under extreme plastic deformation. Proceedings of the national academy of sciences, 201319436 (2014).

7 Misra, A. & Hoagland, R. Effects of elevated temperature annealing on the structure and hardness of copper/niobium nanolayered films. Journal of materials research 20, 2046-2054 (2005).

8 Beyerlein, I. J. et al. Structure–Property–Functionality of Bimetal Interfaces. JOM 64, 1192-1207 (2012).

9 Nizolek, T. et al. Processing and deformation behavior of bulk Cu–Nb nanolaminates. Metallography, Microstructure, and Analysis 3, 470-476 (2014).

10 Misra, A. & Krug, H. Deformation behavior of nanostructured metallic multilayers. Advanced Engineering Materials 3, 217-222 (2001).

11 Raabe, D., Ball, J. & Gottstein, G. Rolling Textures of a Cu--20 Nb Composite. Scripta Metallurgica et Materialia(USA) 27, 211-216 (1992).

12 Hoagland, R., Hirth, J. & Misra, A. On the role of weak interfaces in blocking slip in nanoscale layered composites. Philosophical Magazine 86, 3537-3558 (2006).

13 Abdolrahim, N., Mastorakos, I. & Zbib, H. Deformation mechanisms and pseudoelastic behaviors in trilayer composite metal nanowires. Physical Review B 81, 054117 (2010).

14 Wang, J., Hoagland, R., Hirth, J. & Misra, A. Atomistic modeling of the interaction of glide dislocations with “weak” interfaces. Acta materialia 56, 5685-5693 (2008).

15 Li, N., Wang, J., Huang, J., Misra, A. & Zhang, X. In situ TEM observations of room temperature dislocation climb at interfaces in nanolayered Al/Nb composites. Scripta Materialia 63, 363-366 (2010).

16 Lee, S.-B., LeDonne, J., Lim, S., Beyerlein, I. & Rollett, A. The heterophase interface character distribution of physical vapor-deposited and accumulative roll-bonded Cu–Nb multilayer composites. Acta Materialia 60, 1747-1761 (2012).

17 Misra, A., Hirth, J. & Kung, H. Single-dislocation-based strengthening mechanisms in nanoscale metallic multilayers. Philosophical Magazine A 82, 2935-2951 (2002).

18 Misra, A., Hirth, J. & Hoagland, R. Length-scale-dependent deformation mechanisms in incoherent metallic multilayered composites. Acta materialia 53, 4817-4824 (2005).

19 Nix, W. D. Mechanical properties of thin films. Metallurgical transactions A 20, 2217 (1989).

20 Wang, J., Zhou, C., Beyerlein, I. J. & Shao, S. Modeling interface-dominated mechanical behavior of nanolayered crystalline composites. Jom 66, 102-113 (2014).

21 Mastorakos, I. N., Bellou, A., Bahr, D. F. & Zbib, H. M. Size-dependent strength in nanolaminate metallic systems. Journal of Materials Research 26, 1179-1187 (2011).

22 Abdolrahim, N., Zbib, H. M. & Bahr, D. F. Multiscale modeling and simulation of deformation in nanoscale metallic multilayer systems. International journal of plasticity 52, 33-50 (2014).

23 Martínez, E., Caro, A. & Beyerlein, I. J. Atomistic modeling of defect-induced plasticity in CuNb nanocomposites. Physical review b 90, 054103 (2014).

24 Zhou, J., Averback, R. & Bellon, P. Stability and amorphization of Cu–Nb interfaces during severe plastic deformation: Molecular dynamics simulations of simple shear. Acta Materialia 73, 116-127 (2014).

25 Beyerlein, I. J., Demkowicz, M. J., Misra, A. & Uberuaga, B. Defect-interface interactions. Progress in Materials Science 74, 125-210 (2015).

26 Zhu, Y., Li, Z. & Huang, M. The size effect and plastic deformation mechanism transition in the nanolayered polycrystalline metallic multilayers. Journal of Applied Physics 115, 233508 (2014).

27 Zhu, Y., Li, Z., Huang, M. & Liu, Y. Strengthening mechanisms of the nanolayered polycrystalline metallic multilayers assisted by twins. International Journal of Plasticity 72, 168-184 (2015).

28 Demkowicz, M. & Thilly, L. Structure, shear resistance and interaction with point defects of interfaces in Cu–Nb nanocomposites synthesized by severe plastic deformation. Acta materialia 59, 7744-7756 (2011).

29 Kang, K., Wang, J. & Beyerlein, I. Atomic structure variations of mechanically stable fcc-bcc interfaces. Journal of Applied Physics 111, 053531 (2012).

30 Demkowicz, M., Hoagland, R. & Hirth, J. Interface structure and radiation damage resistance in Cu-Nb multilayer nanocomposites. Physical review letters 100, 136102 (2008).

31 Wang, J. et al. Structure and property of interfaces in ARB Cu/Nb laminated composites. Jom 64, 1208-1217 (2012).

32 Hirth, J. Dislocations, steps and disconnections at interfaces. Journal of Physics and Chemistry of Solids 55, 985-989 (1994).

33 Hirth, J. & Pond, R. Steps, dislocations and disconnections as interface defects relating to structure and phase transformations. Acta Materialia 44, 4749-4763 (1996).

34 Hirth, J., Pond, R. & Lothe, J. Disconnections in tilt walls. Acta Materialia 54, 4237-4245 (2006).

35 Capolungo, L. et al. Dislocation nucleation from bicrystal interfaces and grain boundary ledges: Relationship to nanocrystalline deformation. Journal of the Mechanics and Physics of Solids 55, 2300-2327 (2007).

36 Meyers, M. A., Mishra, A. & Benson, D. J. Mechanical properties of nanocrystalline materials. Progress in materials science 51, 427-556 (2006).

37 Liu, X., Zhang, H. & Lu, K. Strain-induced ultrahard and ultrastable nanolaminated structure in nickel. Science 342, 337-340 (2013).

38 Gianola, D. et al. Stress-assisted discontinuous grain growth and its effect on the deformation behavior of nanocrystalline aluminum thin films. Acta Materialia 54, 2253-2263 (2006).

39 Rupert, T., Gianola, D., Gan, Y. & Hemker, K. Experimental observations of stress-driven grain boundary migration. Science 326, 1686-1690 (2009).

40 Zhu, X. F., Li, Y. P., Zhang, G. P., Tan, J. & Liu, Y. Understanding nanoscale damage at a crack tip of multilayered metallic composites. Applied Physics Letters 92, 1 (2008).

41 Hattar, K. et al. Direct Observation of Crack Propagation in Copper–Niobium Multilayers. Journal of Engineering Materials & Technology 134, 021014 (2012).

42 Zhang, J. Y. et al. Length-scale-dependent deformation and fracture behavior of Cu/ (= Nb, Zr) multilayers: The constraining effects of the ductile phase on the brittle phase. Acta Materialia 59, 7368-7379 (2011).

43 Liang, F., Tan, H. F., Zhang, B. & Zhang, G. P. Maximizing necking-delayed fracture of sandwich-structured Ni/Cu/Ni composites. Scripta Materialia 134, 28-32 (2017).

44 Stukowski, A. Visualization and analysis of atomistic simulation data with OVITO–the Open Visualization Tool. Modelling and Simulation in Materials Science and Engineering 18, 015012 (2009).

45 Plimpton, S. Fast Parallel Algorithms for Short-Range Molecular Dynamics. Journal of Computational Physics 117, 1-19, doi:https://doi.org/10.1006/jcph.1995.1039 (1995).

46 Jones, J. E. On the determination of molecular fields.—II. From the equation of state of a gas. Proc. R. Soc. Lond. A 106, 463-477 (1924).

47 Tersoff, J. New empirical approach for the structure and energy of covalent systems. Physical Review B 37, 6991 (1988).

48 Brenner, D. W. Empirical potential for hydrocarbons for use in simulating the chemical vapor deposition of diamond films. Physical review B 42, 9458 (1990).

49 Foiles, S., Baskes, M. & Daw, M. S. Embedded-atom-method functions for the fcc metals Cu, Ag, Au, Ni, Pd, Pt, and their alloys. Physical review B 33, 7983 (1986).

50 Ziegenhain, G., Hartmaier, A. & Urbassek, H. M. Pair vs many-body potentials: Influence on elastic and plastic behavior in nanoindentation of fcc metals. Journal of the Mechanics and Physics of Solids 57, 1514-1526 (2009).

51 Daw, M. S. & Baskes, M. I. Embedded-atom method: Derivation and application to impurities, surfaces, and other defects in metals. Physical Review B Condensed Matter 29, 6443-6453 (1984).

52 Schiøtz, J., Vegge, T., Di Tolla, F. D. & Jacobsen, K. W. Atomic-scale simulations of the mechanical deformation of nanocrystalline metals. Physical Review B 60, 11971-11983, doi:10.1103/PhysRevB.60.11971 (1999).

53 Kelchner, C. L., Plimpton, S. & Hamilton, J. Dislocation nucleation and defect structure during surface indentation. Physical review B 58, 11085 (1998).

54 Honeycutt, J. D. & Andersen, H. C. Molecular dynamics study of melting and freezing of small Lennard-Jones clusters. Journal of Physical Chemistry 91, 4950-4963 (1987).

55 Kelchner, C. L., Plimpton, S. J. & Hamilton, J. C. Dislocation nucleation and defect structure during surface indentation. Physical Review B 58, 11085-11088 (1998).

56 Frank, F. C. LXXXIII. Crystal dislocations.â□”Elementary concepts and definitions. Philosophical Magazine 42, 809-819 (2010).

57 Zbib, H. M., Rhee, M. & Hirth, J. P. On plastic deformation and the dynamics of 3D dislocations. International Journal of Mechanical Sciences 40, 113–127 (1998).

58 Schwarz, K. W. Local rules for approximating strong dislocation interactions in discrete dislocation dynamics. Modelling & Simulation in Materials Science & Engineering 11, 609 (2003).

59 Schwarz, K. W. Simulation of dislocations on the mesoscopic scale. I. Methods and examples. Journal of Applied Physics 85, 108-119 (1999).

60 Rhee, M., Zbib, H. M., Hirth, J. P., Huang, H. & Rubia, T. D. L. Models for long-/short-range interactions and cross slip in 3D dislocation simulation of BCC single crystals. Modelling & Simulation in Materials Science & Engineering 6, 467 (1999).

61 Fivel, M., Verdier, M. & Canova, G. 3D simulation of a nanoindentation test at a mesoscopic scale. Materials Science & Engineering A s 234–236, 923-926 (1997).

62 Devincre, B. & Kubin, L. Simulations of forest interactions and strain hardening in FCC crystals. Modelling and Simulation in Materials Science and Engineering 2, 559 (1994).

63 Ye, T. THE BOUNDARY ELEMENT METHOD IN ENGINEERING. Acta Aeronautica Et Astronautica Sinica (1987).

64 Ghoniem, N., Tong, S.-H. & Sun, L. Parametric dislocation dynamics: a thermodynamics-based approach to investigations of mesoscopic plastic deformation. Physical Review B 61, 913 (2000).

65 Zhou, C. Dislocation dynamics simulations of plasticity at small scales. (2010).

66 Akarapu, S., Zbib, H. M. & Bahr, D. F. Analysis of heterogeneous deformation and dislocation dynamics in single crystal micropillars under compression. International Journal of Plasticity 26, 239-257, doi:https://doi.org/10.1016/j.ijplas.2009.06.005 (2010).

67 Benzerga, A. A. & Shaver, N. F. Scale dependence of mechanical properties of single crystals under uniform deformation. Scripta Materialia 54, 1937-1941, doi:https://doi.org/10.1016/j.scriptamat.2006.02.003 (2006).

68 Devincre, B., Kubin, L. & Hoc, T. Physical analyses of crystal plasticity by DD simulations. Scripta Materialia 54, 741-746, doi:https://doi.org/10.1016/j.scriptamat.2005.10.066 (2006).

69 Ghoniem, N. M., Tong, S. H. & Sun, L. Z. Parametric dislocation dynamics: A thermodynamics-based approach to investigations of mesoscopic plastic deformation. Physical Review B 61, 913-927, doi:10.1103/PhysRevB.61.913 (2000).

70 Shao, S., Abdolrahim, N., Bahr, D. F., Lin, G. & Zbib, H. M. Stochastic effects in plasticity in small volumes. International Journal of Plasticity 52, 117-132, doi:https://doi.org/10.1016/j.ijplas.2013.09.005 (2014).

71 Zhou, C., Beyerlein, I. J. & LeSar, R. Plastic deformation mechanisms of fcc single crystals at small scales. Acta Materialia 59, 7673-7682, doi:https://doi.org/10.1016/j.actamat.2011.08.032 (2011).

72 Zhou, C., Biner, S. & LeSar, R. Simulations of the effect of surface coatings on plasticity at small scales. Scripta Materialia 63, 1096-1099, doi:https://doi.org/10.1016/j.scriptamat.2010.08.012 (2010).

73 Zhou, C., Biner, S. B. & LeSar, R. Discrete dislocation dynamics simulations of plasticity at small scales. Acta Materialia 58, 1565-1577, doi:https://doi.org/10.1016/j.actamat.2009.11.001 (2010).

74 Balint, D. S., Deshpande, V. S., Needleman, A. & Van, d. G., E. Size effects in uniaxial deformation of single and polycrystals: a discrete dislocation plasticity analysis. Modelling & Simulation in Materials Science & Engineering 14, 409-422 (2006).

75 Schiøtz, J., Di Tolla, F. D. & Jacobsen, K. W. Softening of nanocrystalline metals at very small grain sizes. Nature 391, 561-563, doi:10.1038/35328 (1998).

VITA

Sixie Huang was born in Xin Huang City, Hunan Province, China. He received his Bachelor of Science degree in Polymer Materials and Engineering in June 2013 from Guangdong University of technology, Guangzhou, Guangdong, China. In 2013, Sixie was admitted for Ph.D. in Materials Science and Engineering, Missouri S&T. He commenced his work on his doctoral research project on dislocation dynamics simulation and molecular dynamics of nanolayered composites. In August 2016, he married Youqu Shen, Ph.D. candidate in Materials Science and Engineering Department, Missouri S&T. In June 2017, his first baby, Lilian Huang was born in Rolla, MO, USA. His Ph.D. in Materials Science and Engineering was awarded in May 2019 from Missouri S&T.